JOURNAL OF GEOPHYSICAL RESEARCH, VOL. 114, D01104, doi:10.1029/2008JD010654, 2009

A mechanism for African monsoon breaks: Mediterranean cold air surges

Edward K. Vizy[1,2] and Kerry H. Cook[1,3]

Received 24 June 2008; revised 10 September 2008; accepted 31 October 2008; published 10 January 2009.

[1] Surges of cold air from the Mediterranean into northern Africa during the boreal summer are documented, and their influence on monsoon breaks is analyzed using Tropical Rainfall Measuring Mission rainfall estimates and reanalysis products. Between 1998 and 2006, 6–10 cold air surges occurred each summer, with low-level temperature anomalies ranging from less than −1 K to over −6 K. Composite analysis indicates that cold air surges over northern Africa persist for 2–10 days and travel equatorward at approximately 5.5 m s^{-1}, which is 0.5–1.5 m s^{-1} faster than the observed climatological low-level meridional flow. Northern African cold surges have characteristics similar to surges observed elsewhere in the world, including a hydrostatically induced ridge of surface pressure and an amplified upper tropospheric ridge/trough pattern. The African cold surge is preceded by the passage of a shortwave trough and an intensification of the upper tropospheric subtropical westerly jet streak over the Mediterranean Sea. These events are associated with increased confluence in the jet entrance region over the central Mediterranean, an enhanced direct secondary circulation, subsidence, and low-level ageostrophic northerly flow over northeastern Africa. Composite analysis shows that the passage of a cold surge is associated with an enhancement in convective activity over southern Algeria, western Niger, northern Mali, and Mauritania 2 to 5 days before the surge reaches the eastern Sahel (∼17.5°N), when northeasterly flow channeled between the Atlas and Ahaggar Mountains strengthens and transports relatively moist air from the western Mediterranean and eastern North Atlantic over the region and increases moisture convergence over western Africa north of 20°N. Over the eastern Sahel of Sudan and eastern Chad, the composite results reveal a break in convective activity and decrease in low-level convergence when the surge arrives that persists for about 6 days. These results offer great promise for improving the short-range prediction of rainfall over northern Africa.

Citation: Vizy, E. K., and K. H. Cook (2009), A mechanism for African monsoon breaks: Mediterranean cold air surges, *J. Geophys. Res.*, *114*, D01104, doi:10.1029/2008JD010654.

1. Introduction

[2] Prolonged dry periods during the northern African summer monsoon season can lead to crop failure, food shortages, disease outbreaks, and loss of life and property. Effective subseasonal to interannual weather prediction would greatly improve resource management and disaster preparations. However, a better understanding of the mechanisms associated with synoptic variations in rainfall over northern Africa must first be obtained before weather prediction can be improved.

[1]Department of Earth and Atmospheric Sciences, Cornell University, Ithaca, New York, USA.
[2]Now at Institute for Geophysics, University of Texas at Austin, Austin, Texas, USA.
[3]Now at Jackson School of Geosciences, University of Texas at Austin, Austin, Texas, USA.

0148-0227/09/2008JD010654$09.00

[3] Our current understanding of synoptic rainfall variability is limited over northern Africa. While there have been numerous studies exploring seasonal to decadal rainfall variability over this region [e.g., *Lamb*, 1978; *Folland et al.*, 1986; *Rowell et al.*, 1995; *Ward*, 1998; *Janicot et al.*, 2001], and intraseasonal variability [e.g., *Kiladis and Weickmann*, 1997; *Janicot and Sultan*, 2001; *Sultan et al.*, 2003; *Matthews*, 2004; *Mounier and Janicot*, 2004; *Mounier et al.*, 2008], the mechanisms associated with synoptic fluctuations in rainfall are still not fully understood. Most studies focus on particular aspects such as mesoscale convective systems [e.g., *Laing and Fritsch*, 1993; *Hodges and Thorncroft*, 1997; *Mathon and Laurent*, 2001] and/or easterly wave activity [e.g., *Diedhiou et al.*, 1999; *Berry and Thorncroft*, 2005]. *Bell and Lamb* [2006] examined the relationship between disturbance line variability and intraseasonal to interannual drought over northern Africa and found that the predominant mode of seasonal drought involves near–season long suppression of the seasonal cycle of disturbance line size/organization and intensity,

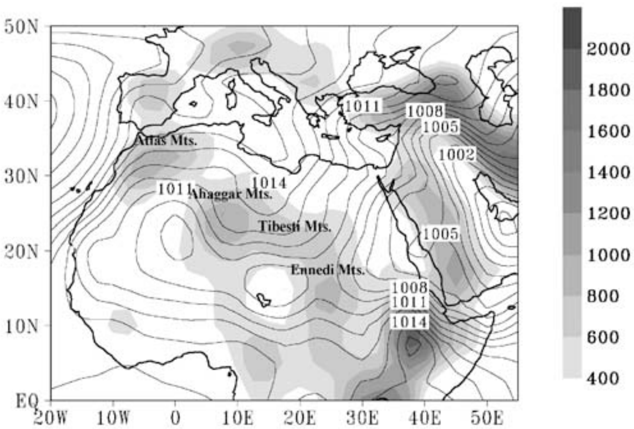

Figure 1. NCEP2 1979–2006 June–August climatological mean sea level pressure (hPa; contours). Contour interval is every 1 hPa. Shading denotes the orographic height in meters as resolved in the NCEP2 reanalysis.

suggesting the importance of variations in the underlying weather systems in influencing northern African drought.

[4] The purpose of this study is to better understand the mechanisms behind African monsoon breaks to improve prediction. In particular, we document the occurrence of cold air surges from Mediterranean midlatitudes during boreal summer, analyze their dynamics, and investigate their influence on precipitation distributions over northern Africa. While we focus on just this one mechanism of variability, we do not imply that other factors are less important in influencing intraseasonal variability over northern Africa. This study is intended to serve as a first step toward understanding monsoon breaks over northern Africa by isolating the role of cold air surges.

2. Background

[5] Boreal summer convection over northern Africa is modulated at the 10–25 and 25–60 day time scales, ‘‘leading to variations of more than 30% of the seasonal signal’’ [*Sultan et al.*, 2003]. The longer time scale modulations, which are substantially weaker than those on the shorter time scale, are likely associated with the remote response to the intraseasonal Madden-Julian oscillation [*Matthews*, 2004].

[6] On the 10–25 day time scale, two independent modes have been identified by *Mounier and Janicot* [2004]. The first mode, called the quasi-biweekly zonal dipole of convection, is characterized by a stationary and uniform modulation of convection, associated with the low-level zonal flow over the equatorial Atlantic and a zonal dipole of convection between Africa and the north equatorial Atlantic near South America. The mechanisms giving rise to this mode are discussed in detail by *Mounier et al.* [2008].

[7] The second 10–25 day mode, or the ‘‘Sahelian mode’’ [*Mounier and Janicot*, 2004; *Mounier et al.*, 2008], is associated with, ‘‘an oscillation between dry and wet conditions that starts in the east and propagates westward over the Sahel, with each phase lasting about 9 days’’ [*Sultan et al.*, 2003]. ‘‘During wet (dry) phases, convection is enhanced (weakened) and its northern boundary moves north (south), while the African easterly jet strength decreases (increases) and the tropical easterly jet strength increases (decreases)’’ [*Sultan et al.*, 2003]. Dry phases are associated with stronger anticyclonic activity over the Sahel, and begin with a, ‘‘slight increase in the negative meridional Ertel potential vorticity gradient at 700 hPa associated with a decrease in the spectral density of African easterly waves’’ [*Lavaysse et al.*, 2006]. Subsidence over the Mediterranean Sea and equatorward advection from midlatitudes may also be playing an important role in this mode [e.g., *Sultan et al.*, 2003], but the mechanisms behind this mode remain unclear.

[8] Here we document the presence of cold air surges over northern Africa, and find that they influence rainfall on submonthly time scales. A cold air surge is a shallow dome of cold, dry air (e.g., $\sim$2 km depth) that advances equatorward, accompanied by a hydrostatically induced ridge of surface pressure and strong meridional low-level winds. Other documented cold surge cases around the world occur to the east of major orographic barriers, including the Rocky Mountains, Andes, and Himalayas [e.g., *Boyle*, 1986; *Tilley*, 1990; *Hartjenstein and Bleck*, 1991; *Schultz et al.*, 1998; *Garreaud*, 2001]. The northern African topography, shown in Figure 1, may not be sufficiently high and uninterrupted in the meridional direction to force cold air surges alone. The Atlas and Ahaggar Mountains of northwestern Africa and the Tibesti and Ennedi Mountains of central Africa do form a chain that tilts from northwest to southeast, and the highest peaks in the Atlas Mountains are over 4 km in height. But most of the orography is 2 km or less and gaps exist between the Atlas and Ahaggar Mountains ($\sim$30°N, 0°E), the Ahaggar and Tibesti Mountains ($\sim$22°N, 10°E), and the Tibesti Mountains and the Ennedi Plateau ($\sim$18°N, 20°E).

[9] Whether generated by topography or synoptic variations (e.g., such as with the development of a cold anticyclone), cold air surges require the presence of a zonally oriented ridge/trough pattern in the middle and upper troposphere. The ridge axis will be located to the west of the low-level surge region [e.g., *Dallavalle and Bosart*, 1975; *Hartjenstein and Bleck*, 1991; *Garcia*, 1996; *Konrad*, 1996]. *Garreaud* [2001] suggests that such an upper level wave pattern can be associated with the passage of extratropical disturbances (i.e., shortwave troughs).

[10] Cold air surges have a major impact on regional climate and rainfall variability. They have profound drying and cooling effects and are a notable sink of energy for the tropics [*Garreaud*, 2001]. The initial advance of cold air can induce a frontal boundary that is favorable for convective development [e.g., *Parmenter*, 1976; *Kousky*, 1979; *Garreaud and Wallace*, 1998; *Liebmann et al.*, 1999]. For example, *Garreaud and Wallace* [1998] estimate that up to 50% of the summertime precipitation over subtropical South America is associated with frontal boundaries ahead of cold air surges.

[11] The seasonality of cold air surges depends on the region. Over North America, they occur mostly during the cold season [e.g., *Murakami and Ho*, 1981; *Bluestein*, 1993],

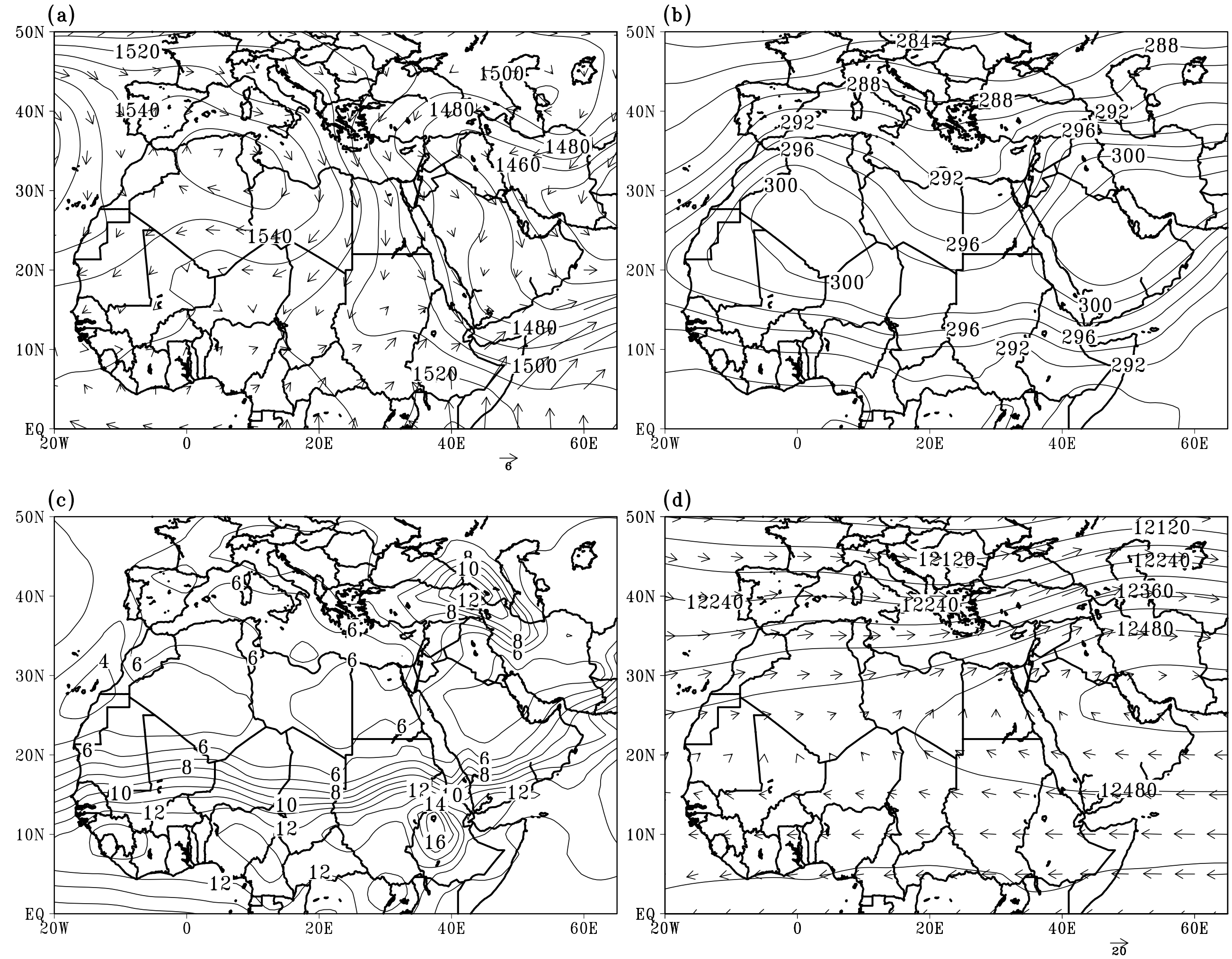

Figure 2. NCEP2 1979–2006 June–August climatological mean sea level pressure (a) 850 hPa geopotential heights (m) and winds (m s^{-1}), (b) 850 hPa air temperature (K), (c) 850 hPa specific humidity (g kg^{-1}), and (d) 200 hPa geopotential heights (m) and winds (m s^{-1}). Contour interval is every 10 m in Figure 2a, 2 K in Figure 2b, 1 g kg^{-1} in Figure 2c, and 60 m in Figure 2d.

but in other regions (e.g., South America) they occur year-round [e.g., *Kousky and Cavalcanti*, 1997; *Krishnamurti et al.*, 1999; *Garreaud*, 2000, 2001].

[12] To our knowledge, the presence of cold air surges over northern Africa has not previously been recognized, though numerous characteristics associated with surges have been described in the literature. For example, *Raicich et al.* [2003] describe a strong equatorward low-level flow over the eastern Mediterranean that penetrates into sub-Saharan Africa. Also, several authors [e.g., *Rodwell and Hoskins*, 1996; *Raicich et al.*, 2003; *Sultan et al.*, 2003] associate Sahel and monsoon rainfall with subsidence over the Mediterranean Sea and, as in *Sultan et al.* [2003], strong low-level northerly flow over northeastern Africa.

[13] *Garreaud* [2001] used the global distribution of the standard deviation of 925 hPa air temperature to identify regions prone to cold air surges. It can be inferred from his results that northeastern Africa may be influenced by these events to some extent in both the summer and winter seasons [*Garreaud*, 2001, Figure 4]. However, his more detailed analysis was restricted to the regions east of the Rockies, Andes, and Himalayas, where topography is more prominent.

[14] *Xoplaki et al.* [2003] relate Mediterranean summer air temperature variations to the large-scale circulation and Mediterranean SSTs during boreal summer using canonical correlation analysis (CCA) of observations and the NCAR/NCEP reanalysis. The negative phase of the second CCA mode, which explains about 24% of the Mediterranean summer air temperature variability, exhibits circulation anomalies typically associated with cold air surges, including an upper tropospheric ridge/trough amplification and higher (lower) 850 hPa heights and warmer (cooler) low-level air temperatures over western (eastern) Europe and the Mediterranean Sea, suggesting that summertime conditions over Northern Africa may be favorable for cold air surges.

[15] In the following section, summertime climatological mean conditions over northern Africa are examined to show that the background climate state associated with cold air surges exists over northern Africa. The cold air surges are

identified in section 4 and, in section 5, a composite surge is analyzed. Results are summarized in section 6.

3. African Summertime Climatological Fields

[16] Figure 1 shows the summertime climatological (1979–2006) mean sea level pressure from the NCEP2 reanalysis [*Kanamitsu et al.*, 2002], featuring relatively high values north of the Atlas Mountains and a broad region of low surface pressure south of the Atlas and Ahaggar Mountains centered along 20°N that extends from the West African coast to the Red Sea and Arabian Peninsula. The high overlies the western Mediterranean, which has surface temperatures 2–10 K cooler than surface temperatures over northern Africa during the summer. The low is the thermal trough that is associated with the warmest summer surface temperature across the northern Sahel, Sahara, and Arabian Desert.

[17] At 850 hPa (Figure 2a), the trough is centered just south of 20°N. High heights are centered over northern Algeria, Tunisia, and northwestern Libya, to the south of the position of the surface high in the summer climatology (Figure 1), setting up a strong height gradient over northeastern Africa between the Atlas Mountains and the Arabian Peninsula. Associated with this gradient, the low-level flow is anticyclonic over much of northern Africa north of 20°N, with strong northerly flow extending from southeastern Europe to Egypt and Libya.

[18] Figure 2b shows the summertime climatological air temperature field at 850 hPa. Warm temperatures associated with the thermal low are present equatorward of the topography of northern Africa. Between the Mediterranean Sea and 20°N, a sharp temperature gradient follows the topography, with isotherms dipping equatorward over Libya and Egypt. The relatively cooler (warmer) air temperatures over northeastern (northwestern) Africa are associated with anticyclonic northerly (southerly) flow (Figure 2a).

[19] Strong meridional moisture gradients characterize the Sahel climate, with specific humidity values decreasing from over 12 g kg^{-1} near 10°N to less than 6 g kg^{-1} north of 20°N (Figure 2c). Over the Sahara (e.g., 20–30°N) and the central Mediterranean Sea, specific humidity values are generally less than 6 g kg^{-1}.

[20] The dominant upper air circulation feature over northern Africa is a large anticyclone that is part of the upper level outflow associated with the Indian monsoon system seen in the 200 hPa flow in Figure 2d. South of this anticyclone, between the equator and 20°N, is strong easterly flow associated with the tropical easterly jet, and to the north (30–45°N) is strong westerly flow associated with the subtropical westerly jet. Note the jet streak extends eastward from 30°E over Asia, with the confluent entrance region over the central and eastern Mediterranean Sea. Summertime climatological wind speeds approach 30 m s^{-1} over eastern Turkey and the Caspian Sea.

[21] In summary, the circulation characteristics often associated with cold air surges are identifiable in the summer climatological mean fields over northern Africa. This includes confluent upper tropospheric flow in the jet entrance region in the vicinity of the trough over the Mediterranean, high surface pressure over northwestern Africa, and strong, equatorward low-level flow over northeastern Africa. This suggests that the large-scale climatological fields over northern Africa may be favorable for the development of cold air surges.

4. Identification of Summertime Cold Air Surges Over Northern Africa

[22] Figure 3 displays Hovmüller diagrams of 850 hPa daily cold temperature anomalies (departures from the 1979–2006 monthly mean climatologies) over northeastern Africa averaged between 10 and 30°E for the summers of 1998–2006. (Note that the warm temperature anomalies have been removed from Figure 3 to focus on the cold anomalies). These summers are chosen to coincide with the TRMM satellite-derived rainfall record [*Huffman et al.*, 2007], since much of the interest in cold surges derives from their influence on rainfall (discussed below). During each of these nine summers, occasional pools of cold air, or cold air surges, move equatorward from the Mediterranean Sea (30–40°N) over northeastern Africa. As listed in Table 1, 77 cold air surges are identified, with 6–10 surge events each summer. Overall, 25 episodes occur in June, 20 in July, 18 in August, and 14 in September. For this count of cold surge events, a cold surge is identified when cool air at 850 hPa propagates equatorward from the Mediterranean Sea (e.g., 30°N, solid line in Figure 3) over northeastern Africa (Figure 3), with no limitation on the propagation speed, the magnitude of the anomaly, or how far equatorward the surge penetrates. More stringent criteria are developed below, to select events relevant for African rainfall. For example, of the 77 events identified in Table 1, about 23% do not reach the eastern Sahel.

[23] There are periods of prolonged cold surge episodes consisting of multiple intrusions (e.g., 1–26 August 2000 and 1–22 July 2006), and times with minimal or no cold air intrusions (e.g., 1–20 July 2002, 15 July to 15 August 2005, 1–31 August 2006, 10–30 September 2006). The anomalies propagate southward at an average speed of 4.24° latitude day^{-1}, or 5.46 m s^{-1}, and those that reach the eastern Sahel do so about 4 to 5 days after cold anomalies first appear over the Mediterranean Sea. Speeds for individual surges range from 2.5° latitude day^{-1} (3.22 m s^{-1}) on 12–17 July 2006 to 6.8° latitude day^{-1} (8.76 m s^{-1}) on 24–25 August 2004, generally faster than the area averaged (15–30°N, 15–30°E) summertime climatological 850 hPa meridional flow of 4 m s^{-1} (3.11° latitude day^{-1}). Note the propagation rates of the surges are calculated as the time difference between when the maximum cooling of an identified surge event is at 30°N and the when the maximum cold temperature anomaly reaches 17.5°N or its southernmost extent for surges that do not reach the eastern Sahel.

5. Composite Analysis of Summertime Cold Air Surges

5.1. Compositing Technique

[24] Now that individual episodes of low-level cold air intrusions over northern Africa have been identified in the reanalysis, the next step is to verify that these episodes share the same circulation characteristics associated with cold air surges discussed in section 2, and investigate their influence

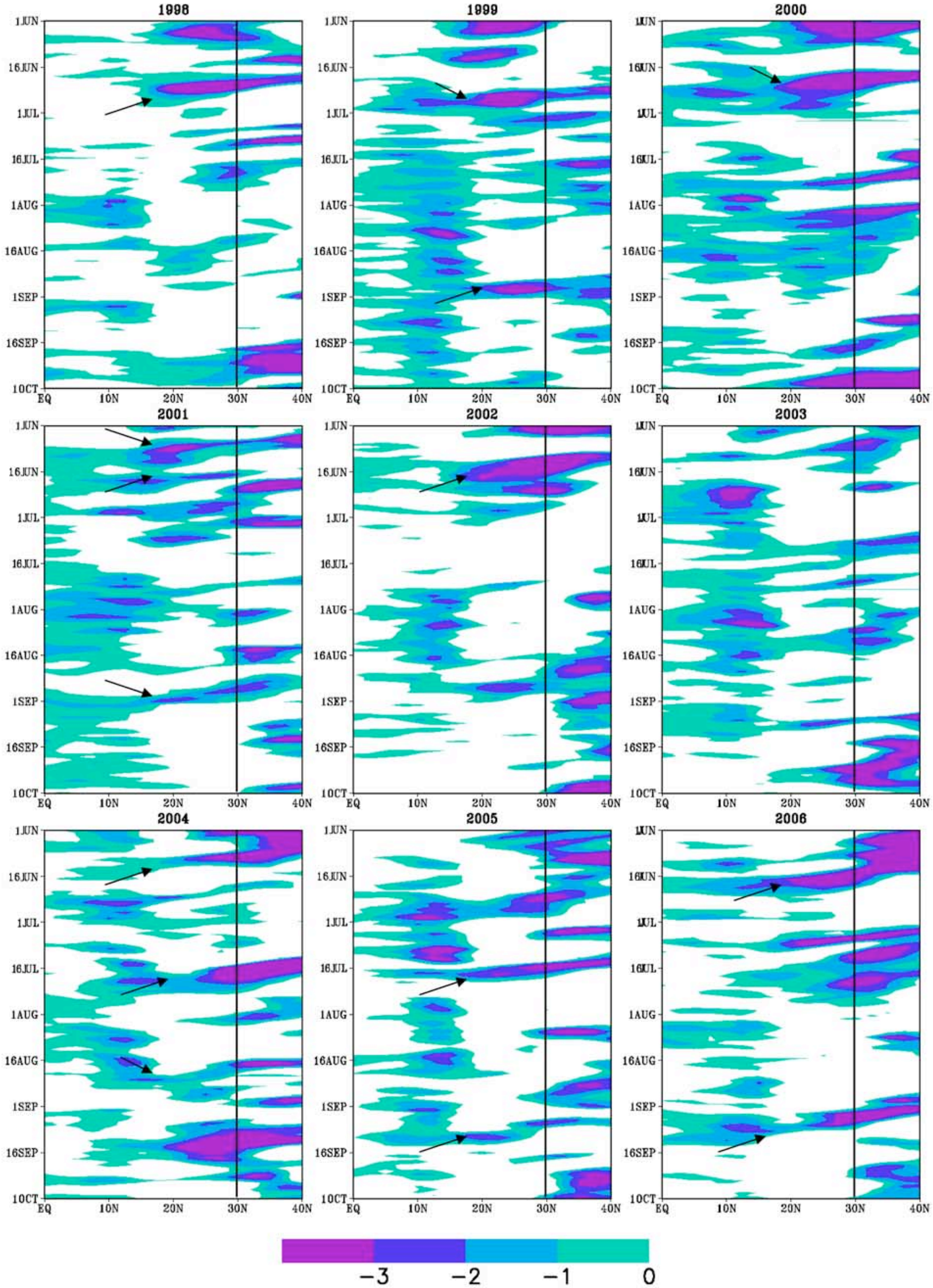

Figure 3. 850 hPa June–September daily cold temperature anomalies (K) averaged between 10 and 30°E for 1998–2006. Anomalies are the daily value minus the 1979–2006 climatological monthly mean value. Arrows denote cold air surge events identified in Table 1 that are used to form the composite. Positive/warm temperature anomalies are not plotted/contoured.

Table 1. Cold Air Intrusions Over Northern Africa Identified From Figure 3[a]

Year	Date When 850 hPa Temperature Anomaly is at 30°N	Maximum 850 hPa Temperature Anomaly (K)	Latitude of Maximum Temperature Anomaly (°N)	Latitude of Furthest Equatorial Extent (°N)	Date When 850 hPa Temperature Anomaly Reaches 17.5°N	Maximum Temperature Anomaly at 17.5°N
1998	2 June	−4.18	22.5	<15	4 June	−1.74
1998	14 June	−1.18	30	22.5	-	-
1998	19 June	−6.41	25	<15	**22 June**	**−2.36**
1998	6 July	−1.86	27.5	20	-	-
1998	10 July	−2.30	30	25	-	-
1998	18 July	−2.44	30	22.5	-	-
1998	11 August	−1.39	30	<15	15 August	−0.94
1998	19 September	−2.53	30	<15	21 September	−0.96
1998	24 September	−1.83	30	<15	26 September	−0.97
1999	1 June	−4.81	22.5	<15	3 June	−1.93
1999	24 June	−4.52	25	<15	**26 June**	**−2.70**
1999	1 July	−2.40	30	20	-	-
1999	18 July	−1.64	25	<15	20 July	−0.87
1999	27 July	−0.87	30	<15	29 July	−0.93
1999	5 August	−2.05	25	<15	6 August	−1.05
1999	25 August	−3.97	27.5	<15	**27 August**	**−2.31**
1999	25 September	−2.30	25	<15	29 September	−0.46
2000	1 June	−6.87	30	<15	4 June	−1.41
2000	8 June	−2.76	25	<15	11 June	−0.78
2000	17 June	−5.91	27.5	<15	**22 June**	**−2.19**
2000	28 June	−3.12	22.5	<15	30 June	−1.91
2000	21 July	−3.63	27.5	<15	24 July	−1.24
2000	1 August	−3.48	30	<15	4 August	−1.88
2000	10 August	−2.30	30	<15	13 August	−1.26
2000	16 August	−2.06	30	<15	19 August	−1.14
2000	14 September	−3.24	27.5	22.5	-	-
2000	24 September	−6.21	30	<15	28 September	−1.04
2001	6 June	−3.82	22.5	<15	**9 June**	**−3.10**
2001	16 June	−2.93	25	<15	**19 June**	**−2.43**
2001	26 June	−2.28	27.5	<15	28 June	−1.32
2001	2 July	−2.65	30	<15	6 July	−1.05
2001	23 July	−1.80	20	<15	26 July	−1.54
2001	1 August	−2.35	30	25	-	-
2001	18 August	−1.68	30	<15	21 August	−0.98
2001	27 August	−2.91	30	<15	**30 August**	**−2.40**
2002	1 June	−5.31	30	17.5	3 June	−0.36
2002	11 June	−4.74	30	<15	14 June	−1.18
2002	17 June	−3.40	27.5	<15	**17 June**	**−2.66**
2002	27 June	−2.14	22.5	<15	29 June	−1.03
2002	22 July	−2.08	25	<15	25 July	−1.20
2002	15 August	−1.04	27.5	<15	17 August	−1.18
2002	23 August	−3.05	22.5	<15	26 August	−1.52
2002	20 September	−1.55	27.5	25	-	-
2003	7 June	−3.33	30	<15	11 June	−0.64
2003	13 June	−1.85	30	22.5	-	-
2003	10 July	−2.10	30	<15	13 July	−0.73
2003	17 July	−1.23	25	<15	19 July	−0.66
2003	22 July	−2.66	30	<15	25 July	−0.94
2003	29 July	−1.07	25	22.5	-	-
2003	7 August	−3.01	30	<15	11 August	−0.81
2003	23 August	−1.46	27.5	20	-	-
2003	6 September	−3.08	25	<15	8 September	−0.39
2003	21 September	−5.61	30	17.5	23 September	−0.38
2004	8 June	−4.18	30	<15	11 June	−0.94
2004	20 June	−2.43	20	<15	**22 June**	**−2.16**
2004	30 June	−1.22	30	<15	2 July	−0.75
2004	15 July	−5.46	30	<15	**20 July**	**−2.17**
2004	1 August	−2.05	30	20	-	-
2004	17 August	−2.96	30	<15	**22 August**	**−2.16**
2004	24 August	−2.05	27.5	<15	25 August	−0.08
2004	4 September	−2.41	27.5	20	-	-
2004	9 September	−6.54	30	<15	12 September	−1.73
2004	22 September	−2.92	30	<15	24 September	−0.20
2005	1 June	−3.63	30	17.5	4 September	−0.45
2005	24 June	−3.51	30	<15	27 June	−1.95
2005	4 July	−2.77	30	27.5	-	-
2005	15 July	−4.22	30	<15	**17 July**	**−2.25**
2005	5 August	−3.17	30	27.5	-	-
2005	26 August	−1.99	30	27.5	-	-
2005	5 September	−3.33	30	<15	**9 September**	**−2.01**

Table 1. (continued)

Year	Date When 850 hPa Temperature Anomaly is at 30°N	Maximum 850 hPa Temperature Anomaly (K)	Latitude of Maximum Temperature Anomaly (°N)	Latitude of Furthest Equatorial Extent (°N)	Date When 850 hPa Temperature Anomaly Reaches 17.5°N	Maximum Temperature Anomaly at 17.5°N
2006	16 September	−1.94	30	25	-	-
2006	8 June	−2.89	30	<15	11 June	−0.19
2006	14 June	−4.71	25	<15	**17 June**	**−2.48**
2006	6 July	−4.51	27.5	<15	8 July	−1.67
2006	12 July	−4.55	30	<15	17 July	−1.62
2006	20 July	−4.32	30	20	-	-
2006	2 September	−4.38	30	<15	**6 September**	**−2.26**

[a]Bold typing denotes events used to formulate the composite.

on the moisture and precipitation over northern Africa. To do so, a composite surge event is constructed.

[25] Two criteria are used to define the selection of cold air surge events for the composite. First, only cases in Figure 3 in which the 850 hPa cold temperature anomalies moving equatorward from 30°N (solid black line in Figure 3) that reach 17.5°N are included. 59 of the 77 events listed in Table 1 meet this criterion. Second, relatively strong events are selected, i.e., those with temperature anomalies of −2°C or greater at 17.5°N. This temperature threshold is selected because it corresponds to approximately 1.5 standard deviations away from the climatological monthly mean at 17.5°, while this threshold approach is adopted to keep the analysis objective. Note that by doing so, some potential case events that could be relevant may be excluded. Of the 59 remaining events, about 25% or 15 events meet this criterion. These events used in the composite are denoted in Table 1 by bold type in the last two columns and the black arrows in Figure 3.

[26] The selected strong cold surge case studies are aligned with day 0 corresponding to the date when the 850 hPa maximum temperature anomaly reaches 17.5°N. The sixth column in Table 1 lists these dates.

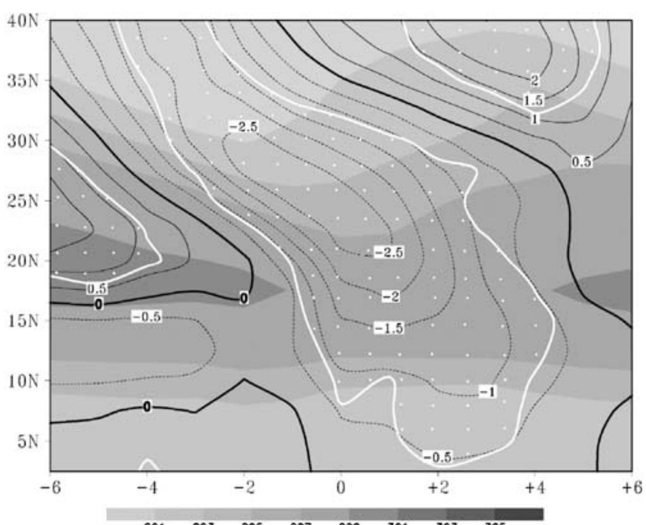

Figure 4. Composite 850 hPa temperature (K; shaded), and temperature anomaly (K; black contoured) averaged between 10 and 30°E for the 15 cold air surge case studies listed in Table 1. Horizontal axis denotes time in days from the composite center. Temperature anomalies significant at the 95% level are stippled.

5.2. Composite Results

5.2.1. Low-Level Results

[27] Figure 4 shows the evolution of the 850 hPa temperature and temperature anomaly fields of the composited cold air surge averaged between 10 and 30°E. The temperature anomalies are calculated as the difference from the appropriate climatological monthly mean value to decrease the influence of seasonality. The calculated composited

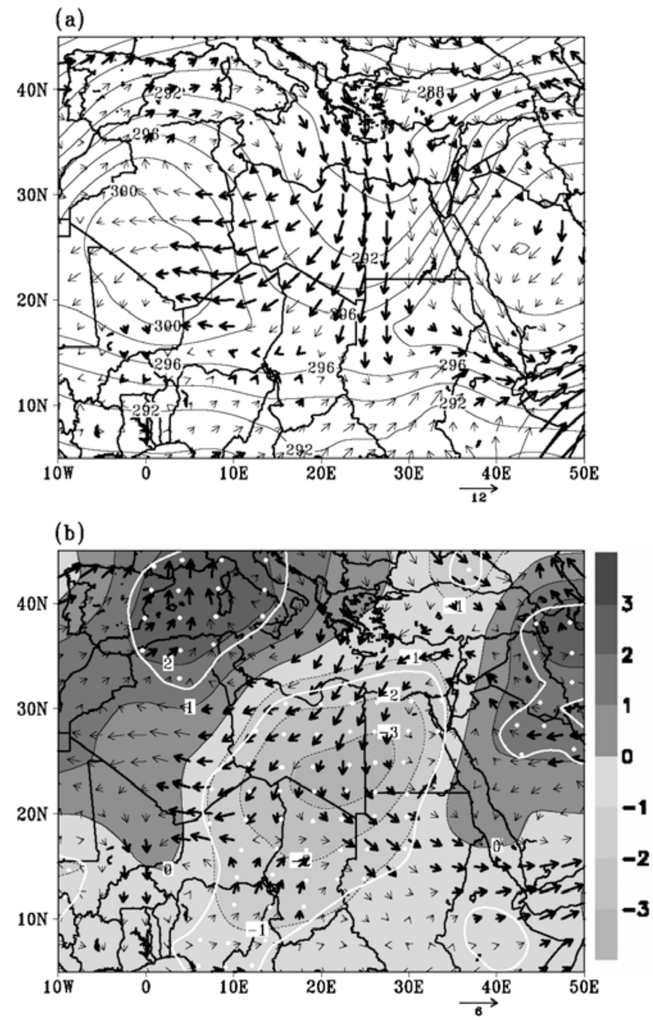

Figure 5. Composite 850 hPa (a) temperature (K) and winds (m s^{-1}) and (b) temperature and wind anomalies for day 0. Wind and wind anomaly arrows locally significant at the 95% are bold, while temperature anomalies locally significant at the 95% level in Figure 5b are stippled.

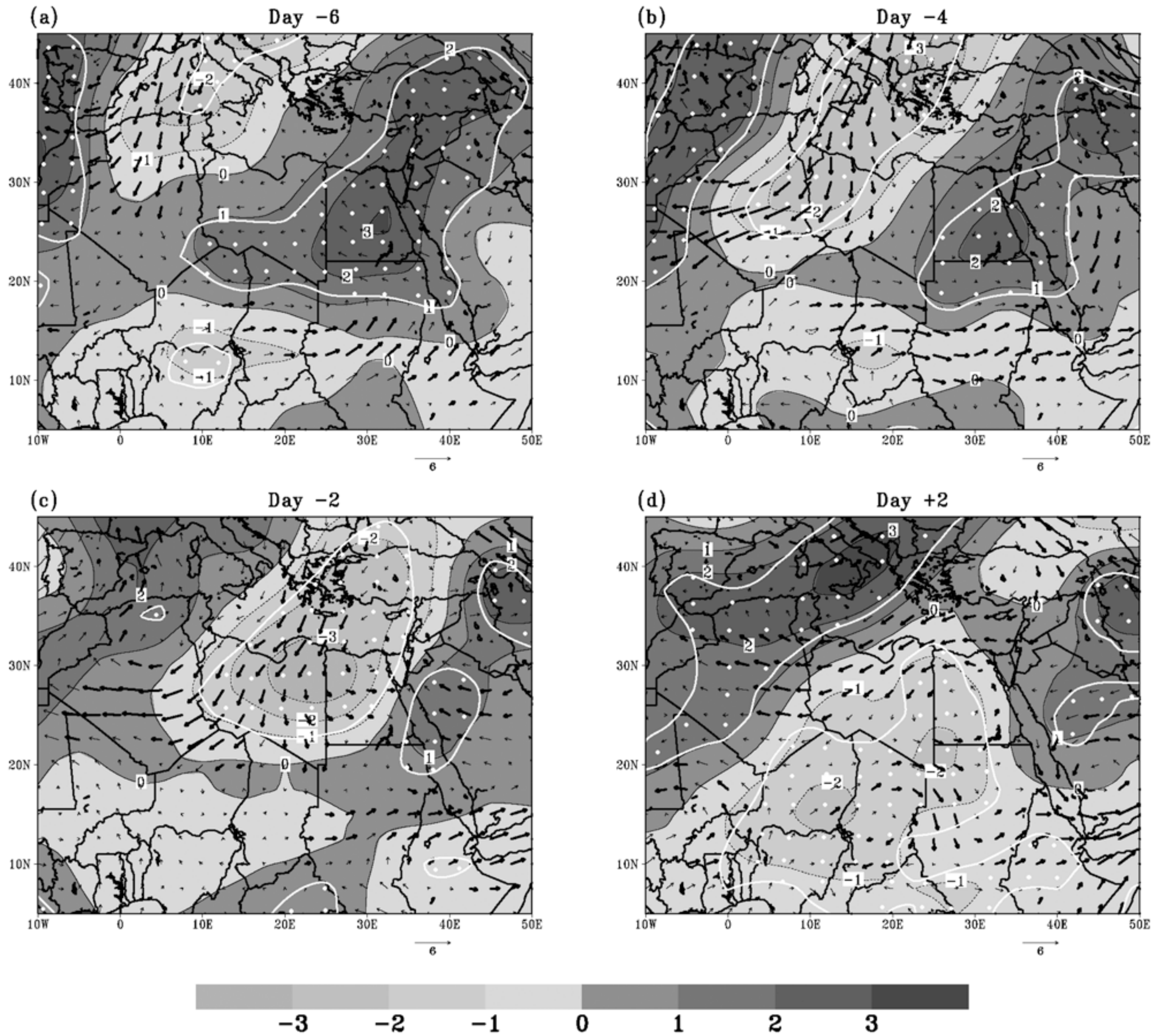

Figure 6. Composite 850 hPa daily temperature (K) and winds (m s^{-1}) anomalies for (a) day −6, (b) day −4, (c) day −2, and (d) day +2. Contour interval is every 1 K. Wind and wind anomaly arrows locally significant at the 95% are bold, while temperature anomalies locally significant at the 95% level are stippled.

propagation speed from the Mediterranean Sea (~30°N) to the Sahel (~15°N) is 3.75° latitude day^{-1}, or 4.81 m s^{-1}, approximately 20% stronger than the climatological summertime 850 hPa meridional flow. Interpreting the propagation speed from Figure 4 yields rates ranging from 3.75° latitude day^{-1} to 7.50° latitude day^{-1} depending on which contour is utilized. Note that even though there is some uncertainty in the rate calculation, all of the rates are larger than the climatological meridional flow rate by at least 20%. From day −6 to day 0, 850 hPa temperatures over northeastern Africa drop 1–4.5 K. The cooler air temperatures persist approximately 4 days over the eastern Sahel (10–20°N) and are generally confined below 650 hPa, with the coldest anomalies close to the surface. Over the Mediterranean Sea (30–40°N) temperatures warm by 2.5 K between day 0 and day +4 immediately following the surge of cold air. Values significant at the 95% level are stippled (see Appendix A for details of how significance is determined).

[28] Figures 5a and 5b show the day 0 composite 850 hPa temperature and wind fields and their anomalies, respectively. Compared to the summer climatology (Figure 2), 850 hPa air temperatures are more than 3 K cooler over northeastern Africa and 2 K warmer over the western Mediterranean Sea at this time. This amplified isotherm pattern (Figure 5a) is associated with a stronger anticyclone over northern Algeria, Tunisia, and western Libya with anomalously northerly (southerly) flow advecting relatively cooler (warmer) air equatorward (poleward) over the eastern Mediterranean Sea and northeastern Africa (western Mediterranean Sea and northern Algeria).

[29] Figures 6a–6c show the 850 hPa temperature and wind anomalies that precede the arrival of the surge at 17.5°N. Six days earlier (day −6; Figure 6a) a cold

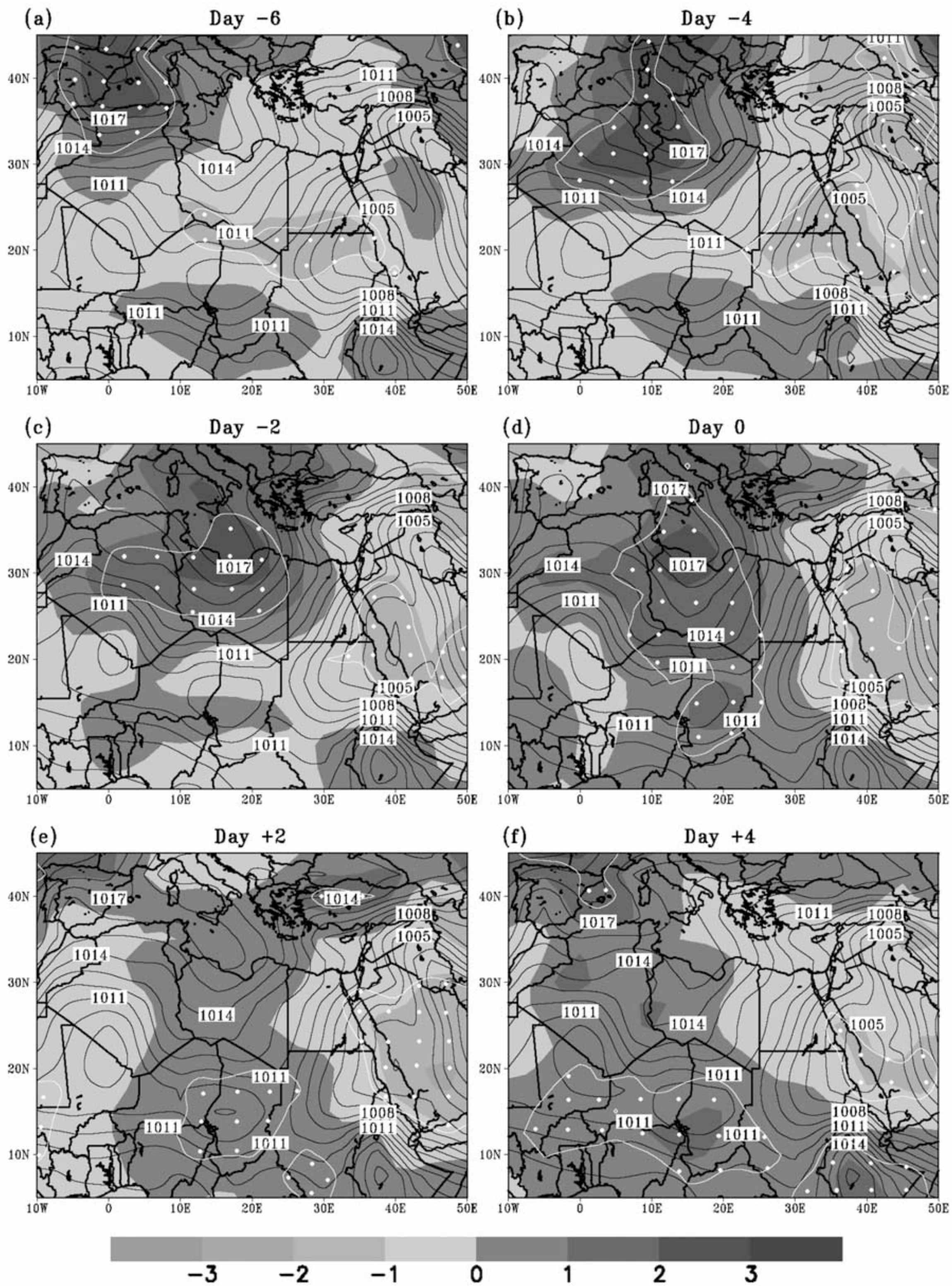

Figure 7. Composite mean sea level pressure (contours) and mean sea level pressure anomalies (shading) for (a) day −6, (b) day −4, (c) day −2, (d) day 0, (e) day +2, and (f) day +4. Contour interval is every 1 hPa. Shading is in hPa according to the scale at the bottom. Anomalies locally significant at the 95% level are stippled.

temperature anomaly of over −2 K is situated just north of the Algerian/Tunisian coast in association with anomalous northerly flow over the western Mediterranean Sea and northern Algeria. An anticyclonic anomaly is located over Spain (not shown), to the northwest of the climatological anticyclone over western Algeria (Figure 2a). The statistically significant anomalous northerly flow is the eastern flank of the anticyclone, which is advecting cooler air equatorward. The low-level flow shifts and becomes northerly over the Atlas Mountains at this time (not shown), which is a reversal of the summer climatological wind direction (see Figure 2a).

[30] By day −4 (Figure 6b) the cool air anomaly has advanced to the south and east, with cold anomalies over −2 K extending from the central Mediterranean Sea to northwestern Libya, Tunisia, and southeastern Algeria associated with anomalous northerly/northeasterly flow. The gap between the Atlas and Ahaggar Mountains seems to channel flow into southern and central Algeria. Low-level wind speeds double, advecting colder air associated with the surge southwestward over southern Algeria. Over Spain, warm temperature anomalies over +2.5 K are associated with anomalous southerly flow in the wake of the low-level anticyclone.

[31] By day −2 (Figure 6c), the cold temperature anomalies and anomalous northerly flow are located over Libya and Egypt, extending equatorward to the Ahaggar and Tibesti Mountain ranges at approximately 22°N (Figure 1). Anomalous northerly flow remains strong over Libya instead of shifting eastward. Anomalous warming continues over the western Mediterranean Sea, and is associated with an enhanced southerly flow around the western flank of the low-level anticyclone.

[32] As discussed earlier, the pool of cold air associated with the cold air surge reaches the eastern Sahel on day 0 (Figure 5b), and by day +2 (Figure 6d) the cold air remains in place over eastern North Africa, but in a weakened state with temperature anomalies approximately 1 K smaller. Anomalous northerly flow has also weakened considerably over northeastern Africa, with the strongest anomalies located over western Sudan, due east of the Ennedi Mountains. Over the Mediterranean, warm anomalies from the west are advected eastward by the westerly flow along the northern flank of the low-level anticyclone (Figure 2a), resulting in low-level warming over the eastern Mediterranean following the passage of the cold air surge (see Figure 4). The anomalous cooling over northeastern Africa continues to weaken over the next 3–4 days (not shown), as conditions return to normal (Figure 2).

[33] Figure 7 depicts the evolution of the sea level surface pressure field and its anomalies during the composited cold air surge. On day −6 (Figure 7a), a surface ridge is centered at approximately 40°N and 0°E, with sea level pressure anomalies of more than 3 hPa. To the south, the thermal low extends across the continent between 15 and 22°N, with anomalies of −1 to −2 hPa over northern Chad and Sudan. The stronger thermal trough over eastern Africa is accompanied by anomalous westerly/southwesterly flow on its southern boundary over central Chad and Sudan (Figure 6a).

[34] On day −4 (Figure 7b), the anticyclone has moved to just east of the Atlas Mountains, centered over Tunisia with a maximum pressure of 1018 hPa, and anomalies of 3–4 hPa. Sea level pressure has risen over northwestern Libya and much of Algeria. The thermal low remains anomalously strong, while the thermal low over the Arabian Peninsula and Middle East deepens by 1 to 2 hPa. The surface pressure gradient strengthens over northeastern Africa between the anticyclone over the western Mediterranean Sea region and the thermal low to the south over the Sahara and to the east over the Arabian Peninsula. The thermal low begins to weaken over Chad, but surface pressure anomalies still remain significant over Sudan, with strong anomalous westerly flow along its southern boundary (Figure 6b).

[35] By day −2 (Figure 7c), the anticyclone has expanded over the western and central Mediterranean Sea and northwestern Africa, with pressure rises of 1–2 hPa reaching the Ahaggar and Tibesti Mountains. The center of the anticyclone remains anchored over the Mediterranean Sea, where water surface temperatures are cooler than the adjacent land surface temperatures by 2 to 8 K. While the thermal trough over continental Africa and the thermal low over the Arabian Peninsula remain 1–2 hPa stronger than the climatological average, maintaining the strong surface pressure gradient over northeastern Africa, the anomalies are no longer statistically significant over Chad and Sudan.

[36] On day 0 (Figure 7d), the anticyclone is centered just north of the Libyan coast, with mean sea level pressure over much of northern Africa anomalously high. This includes the central African thermal trough region between 5 and 30°E, where mean sea level pressure anomalies are from 0.2 to 1.2 hPa. To the east, the thermal low over the Arabian Peninsula and, thereby, the pressure gradient over eastern Libya and Egypt remain strong.

[37] By day +2 (Figure 7e) the high-pressure system has retreated to the north and west, and it is located over the western Mediterranean Sea by day +4 (Figure 7f). The thermal trough remains weaker than normal through day +4.

[38] The results from Figures 4–7 indicate that temperature drops of 3–4 K, and pressure rises of 1–2 hPa are associated with northern African cold air surges. While these values are much smaller than those associated with wintertime cold air surges elsewhere [e.g., *Colle and Mass*, 1995; *Schultz et al.*, 1998; *Garreaud*, 1999], they are comparable to the South American summertime surge anomalies of −4 K, with 2 hPa pressure rises [*Garreaud and Wallace*, 1998].

5.2.2. Precipitation

[39] Of great importance is the ability of African cold air surges to trigger monsoon breaks, so TRMM rainfall rates are examined. Figure 8a shows composited daily TRMM rainfall rates along with 850 hPa wind anomalies for day −6. On day −6, rainfall is widespread across the continent between 5 and 15°N. North of 15°N over the northern Sahel and southern Sahara, there are sporadic clusters of convective activity from Mauritania in the west to Chad in the east.

[40] Figure 8b shows the 850 hPa specific humidity anomalies from the composite on day −6. Low-level moisture values over Algeria, northern Niger, and Mali are 0.5–1 g kg^{-1} above the climatological mean, representing a 5–15% increase in the low-level moisture content over this relatively dry region (Figure 2c). Over the eastern Sahel, in Chad and Sudan, the low-level moisture anomaly is also positive, with specific humidity anomalies exceeding 1 g kg^{-1}. The increase in low-level moisture over the

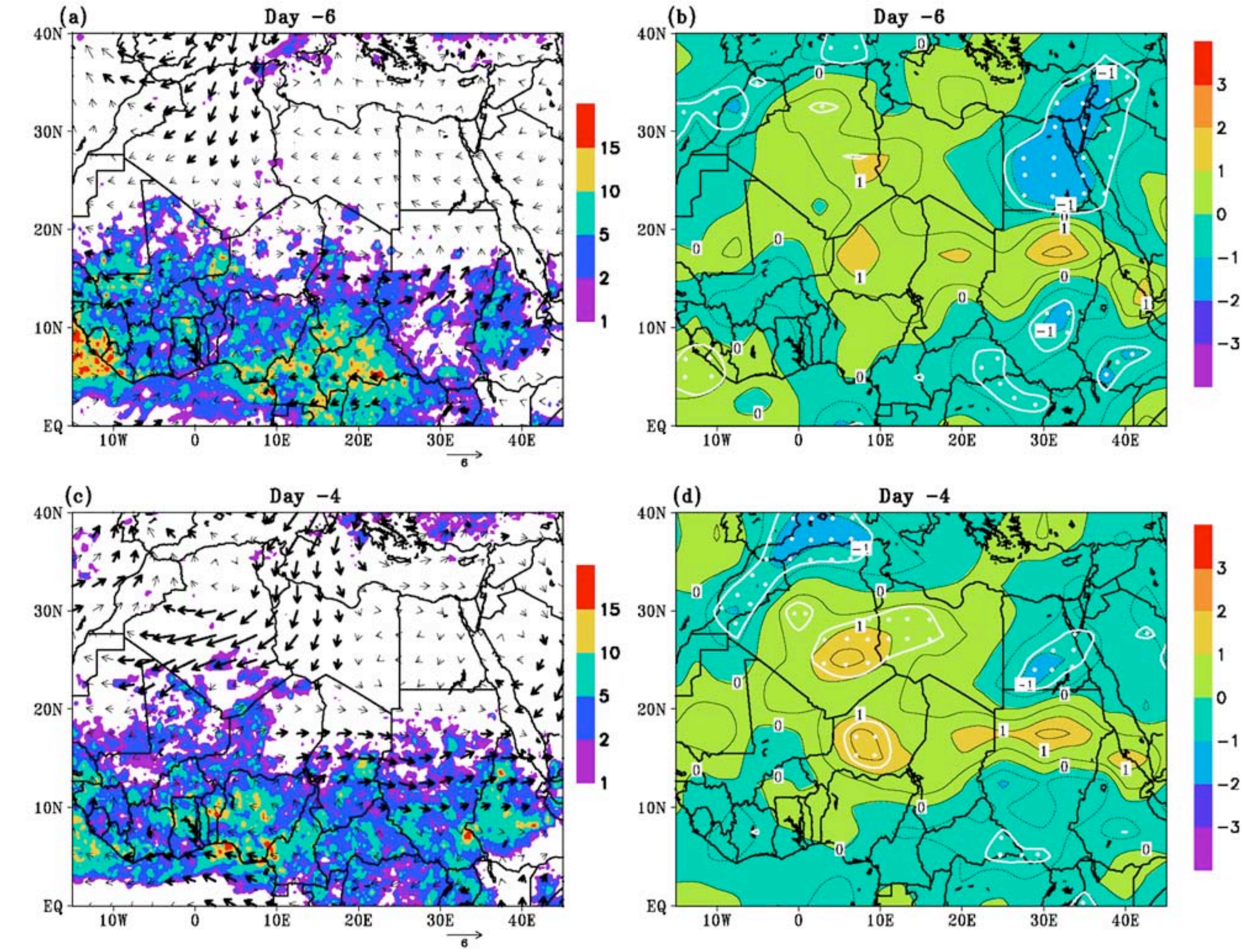

Figure 8. Composite daily (a) rainfall rate (mm day^{-1}) and 850 hPa wind anomalies (m s^{-1}) and (b) 850 hPa specific humidity (g kg^{-1}) anomalies for day −6. Composite daily (c) rainfall rate and 850 hPa wind anomalies and (d) 850 hPa specific humidity anomalies for day −4. Contour interval is every 0.5 g kg^{-1} in Figures 8b and 8d. Wind anomaly arrows locally significant at the 95% level are bold, while specific humidity anomalies locally significant at the 95% level are stippled.

eastern Sahel is associated with a stronger African monsoon trough (Figure 7a) positioned a few degrees of latitude further north than normal (Figure 1) and anomalous westerly/southwesterly flow with enhanced (weaker) low-level convergence over northern (southern) Chad and Sudan (not shown, but interpreted from Figures 2a and 7a). 850 hPa moisture convergence over northern Sudan is approximately double the climatological mean value at this time and is reduced by 80–110% over southern Sudan (not shown). In contrast, the increase in moisture over the western Sahara is associated with both a northward shift of the monsoon trough as well as an increase in the low-level moisture associated with the anomalous northerly flow from the western Mediterranean and southwestern Europe. Low-level moisture convergence also increases by 50–75% over southern Algeria (not shown), just ahead of the anomalous northerly cold air surge boundary (i.e., at the southern boundary of the significant wind anomaly vectors over Algeria in Figure 8a).

[41] By day −4 convective activity over southern Algeria, northern Niger, and northern Mali intensifies (Figure 8c) as anomalous northerly/northeasterly flow associated with the cold air surge is channeled through the gap in the topography between the Atlas and Ahaggar Mountains of Algeria. The low-level moisture content of the atmosphere increases by 25–35% over southern Algeria at this time (Figure 8d), associated with the doubling in strength of the channeled flow between the orography over Algeria and the continued anomalous northward shift of the summer monsoon trough across continental Africa. Low-level moisture convergence also doubles over southeastern Algeria at this time (not shown), in the region where the anomalous northerly/northeasterly flow begins to weaken (Figure 8c). Note that the cold air surge only extends to approximately 20°N over the western Sahara, approximately 5° to 10° of latitude north of the primary summertime land-based convergence zone over West Africa, suggesting that the cold air surges may not have a strong interaction with this convergence

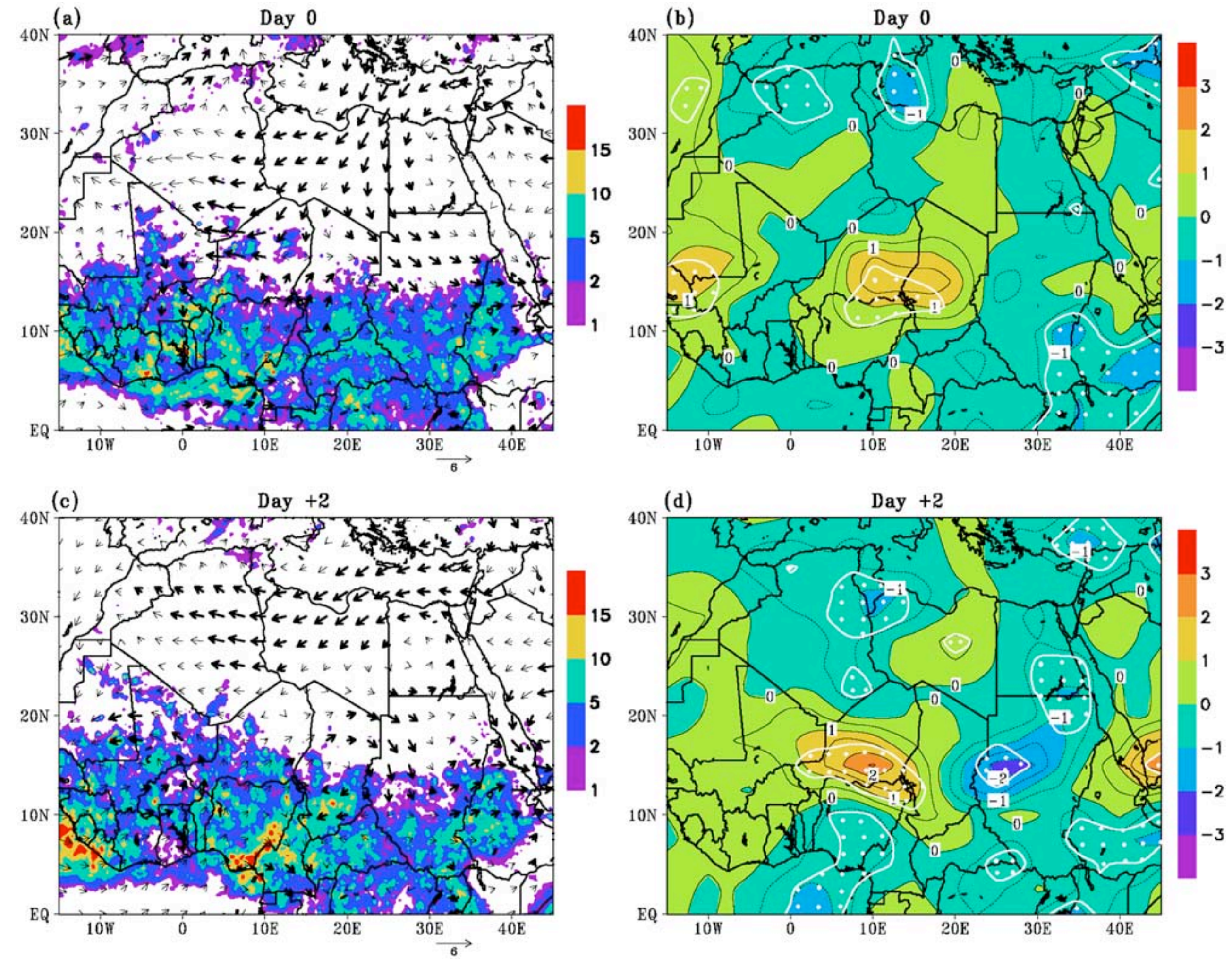

Figure 9. Composite daily (a) rainfall rate (mm day^{-1}) and 850 hPa wind anomalies (m s^{-1}) and (b) 850 hPa specific humidity (g kg^{-1}) anomalies for day 0. Composite daily (c) rainfall rate and 850 hPa wind anomalies and (d) 850 hPa specific humidity anomalies for day +2. Contour interval is every 0.5 g kg^{-1} in Figures 9b and 9d. Wind anomaly arrows locally significant at the 95% level are bold, while specific humidity anomalies locally significant at the 95% level are stippled.

zone over the western Sahara. This enhancement of convective activity north of 20°N is short lived, as by day −2 rainfall rates and the positive low-level specific humidity anomalies decrease in magnitude (not shown).

[42] The influence of the cold air surge on rainfall over the eastern Sahel is opposite to the response over the Western Sahara, with a 4–6 day break in rainfall over Sudan and Chad beginning on day 0. Figure 9a shows the composited daily TRMM rainfall rates and 850 hPa wind anomalies for day 0. Convective activity that extended to 19°N over Sudan and Chad four days earlier has retreated equatorward and is now south of 15°N. This retreat is associated with anomalous low-level northwesterly flow over northern Chad and Sudan, as cooler, drier air from the north is transported equatorward around the topography of the Tibesti and Ennedi Mountains.

[43] Figure 9b shows the 850 hPa specific humidity anomaly for day 0. The strong positive low-level moisture anomaly over Sudan on day −4 (Figure 8d) has weakened and retreated equatorward, replaced by weak negative moisture anomalies generally less than 0.5 g kg^{-1} over northern Sudan. This change in the moisture anomaly indicates an equatorward retreat of the meridional moisture gradient over the eastern Sahel (Figure 2c). Large positive moisture anomalies persist over Chad, northern Nigeria, and Niger in regions to the south and west of the main topography features (Figure 1), suggesting that orography may shield Central Africa from strong dry air intrusions to some degree, and/or the influence of the low-level southwesterly flow associated with the West African monsoon may play a dominant role in transporting moisture into this region. These moisture anomalies could also be a consequence of strong moisture convergence prior to day 0. It is unclear from this analysis what role the cold air surge may be having in the increase in low-level moisture and convective activity over the central Sahel.

[44] By day +2 (Figure 9c), rainfall rates continue to decrease over the eastern Sahel (Sudan and eastern Chad), with convective activity weakening as far south as 10°N. This break/weakening of convective activity is associated

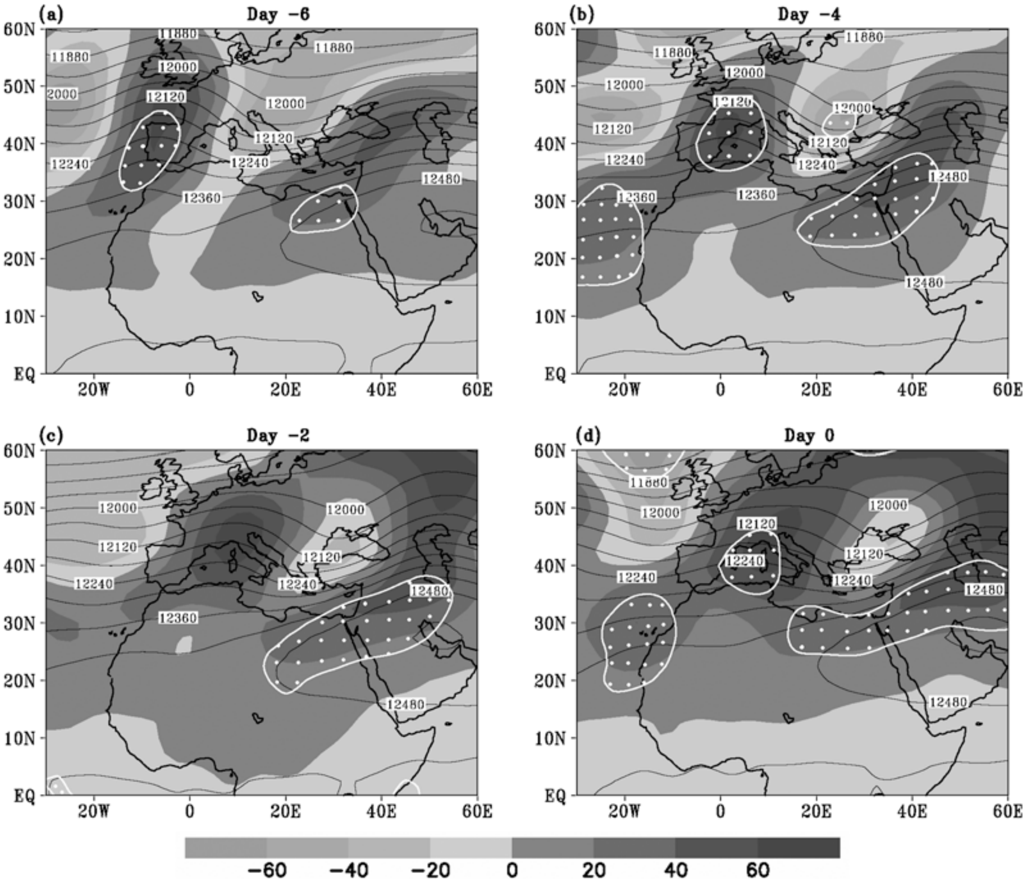

Figure 10. Composite 200 hPa geopotential heights (contours) and geopotential height anomalies from weighted climatology (shading) for (a) day −6, (b) day −4, (c) day −2, and (d) day +0. Contour interval is every 60 m. Shading is in meters according to the scale at the bottom. Height anomalies locally significant at the 95% level are stippled.

with anomalous northerly flow east of the Ennedi Mountains of eastern Chad. To the west, convective activity remains strong south of 15°N over southern Chad, Niger, Nigeria, and Cameroon.

[45] Figure 9d shows the 850 hPa specific humidity anomaly for day +2. Drying over the eastern Sahel of Sudan has increased, with specific humidity anomalies of -2 g kg^{-1} or greater, a 20–30% reduction compared with the climatological mean. To the west, specific humidity ratios increase by 2 g kg^{-1} over Niger, and are associated with increased convective activity and anomalous southwesterly low-level flow (Figure 9c). This anomalous low-level moisture pattern remains in place until day +6 (not shown), but with magnitudes gradually weakening from their peak at day +2. Similarly, rainfall remains below normal over central Sudan and eastern Chad through day +6 (not shown).

[46] Over eastern Africa the cold air surge extends to 10°N, about 10° of latitude further south than the surge reached over western Africa. In doing so, the surge extends south of the driest part of eastern Sahara desert (Figure 2c). The anomalous northerly flow shown in Figure 9 over the eastern Sahel is associated with the advection of relatively drier air from the eastern Sahara and weaker convergence over the eastern Sahel.

[47] Note TRMM rainfall rates involve a complex algorithm that blends satellite and ground-based observational rainfall estimates to formulate an end product rainfall rate, and that there are relative errors involved in the algorithm process. Results discussed above may be dependent upon the use of the TRMM rainfall rates.

5.2.3. Upper Level Conditions Associated With the Cold Air Surge

[48] Figure 10 shows the composite height and height anomalies at 200 hPa. A ridge/trough pattern is discernable at this level on day −6 (Figure 10a) with confluent flow implied by the strengthening of the geopotential gradients east of the ridge axis over the central Mediterranean Sea. The composited results for day −7 (not shown) indicate that the development of the trough at 200 hPa east of the ridge axis precedes the development of a trough at 500 hPa by 1 day, indicating that the development of the 500 hPa trough and cold air surges may be forced from upper tropospheric changes.

[49] By day −4 (Figure 10b) the ridge and trough axes have moved eastward by approximately 10°. Heights associated with the ridge (trough) axis at 0°E (30°E) are 60–80 m above (below) normal and are at their greatest magnitudes in the composite. Associated with this amplified pattern is

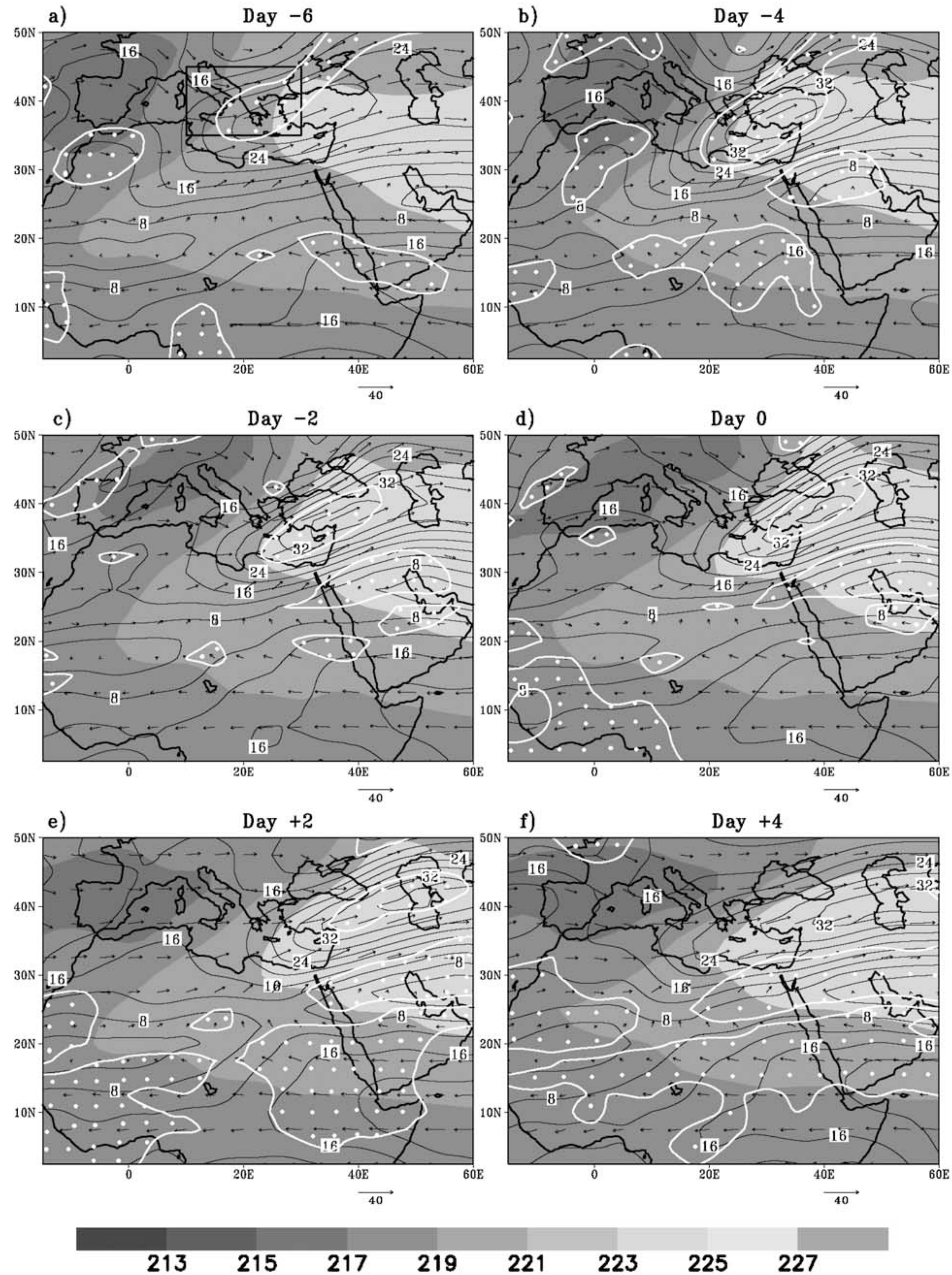

Figure 11. Composite 200 hPa daily isotachs (m s^{-1}; contoured), temperature (K; shaded), and wind vectors (m s^{-1}) for (a) day −6, (b) day −4, (c) day −2, (d) day +0, (e) day +2, and (f) day +4. Contour interval is every 4 m s^{-1}. Isotachs locally significant at the 95% level are stippled. The box in Figure 11a denotes the averaging region over the Mediterranean used in Figure 12.

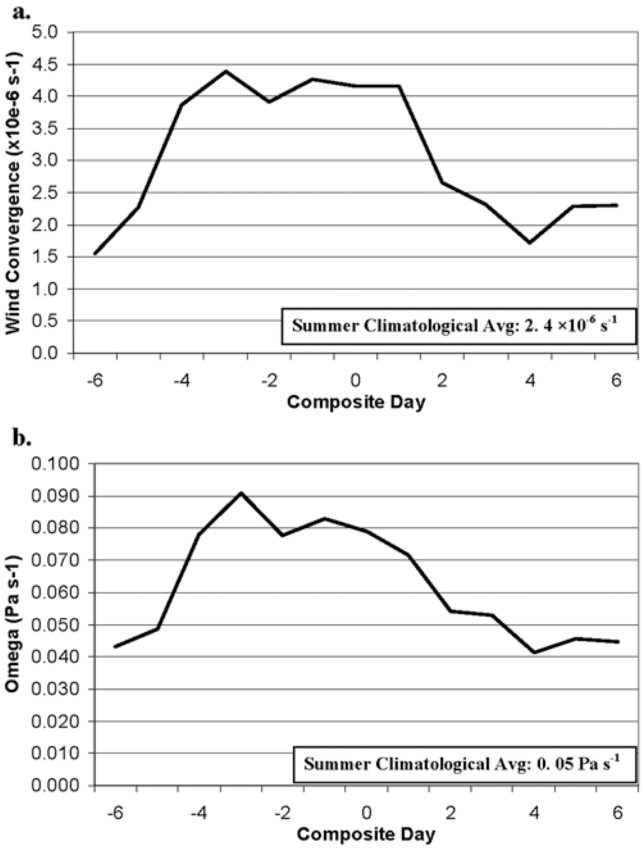

Figure 12. Composite (a) 200 hPa wind convergence ($\times\ 10^6\ s^{-1}$), and (b) 500 hPa vertical p velocity (Pa s) area averaged between 10 and 30°E and 35 and 45°N. Horizontal axis denotes time in days from the composite center (0).

strong confluence over the central and eastern Mediterranean Sea.

[50] The trough begins to weaken by day −2 (Figure 10c), while the ridge axis remains 60–80 m stronger than average until day 0 (Figure 10d), after which it weakens. By day +2 (not shown), the 200 hPa height field resembles the summertime climatology (Figure 2d).

[51] The development of the upper tropospheric amplified ridge/trough pattern and strengthening of the confluence over the Mediterranean Sea is associated with an intensification of the subtropical westerly jet. Figure 11 shows the composited isotachs, wind vectors, and temperature at 200 hPa. A westerly jet streak with a maximum of 30 m s^{-1} is present over the eastern Mediterranean Sea, Turkey, and western Asia on day −6 (Figure 11a) with the jet entrance region positioned over the central Mediterranean Sea. The jet streak intensifies to over 36 m s^{-1} as the 200 hPa shortwave trough deepens over the eastern Mediterranean Sea on day −4 (Figure 11b). The jet core remains strong (e.g., greater than 36 m s^{-1}) on day −2 (Figure 11c) and begins to move northeastward on day 0 (Figure 11d), associated with the passage of the upper level shortwave trough. The jet streak remains over western Asia on day +2 and day +4 (Figures 11e and 11f), with maximum wind speeds dropping below 36 m s^{-1}.

[52] The passage of a shortwave trough in the upper tropospheric flow has been associated with cold air surges in other regions [e.g., *Chang and Lau*, 1980; *Lau et al.*, 1983; *Chu and Park*, 1984; *Boyle*, 1986; *Schultz et al.*, 1997, 1998]. Similar to other jet entrance regions, the confluent upper tropospheric jet entrance region over the Mediterranean Sea is associated with a direct secondary circulation that favors upper level wind convergence and subsidence, and increased ageostrophic southerly (northerly) flow in the upper (lower) levels over the central and eastern Mediterranean Sea and northern Africa [*Beebe and Bates*, 1955; *Uccellini and Johnson*, 1979]. As the shortwave trough deepens by day −4, the upper level confluence and subsidence increase and the direct secondary circulation intensifies.

[53] Figure 12a shows the 200 hPa composited wind convergence in the left entrance region of the subtropical westerly jet (10–30°E, 35–45°N). On day −6, the upper level wind convergence is below the climatological summer average of $2.4 \times 10^{-6}\ s^{-1}$, but increases abruptly on day −4 to about $4.0 \times 10^{-6}\ s^{-1}$ and remains high through day +1. This represents a 70–90% increase in wind convergence in the left entrance region of the upper level westerly jet.

[54] Figure 12b shows the 500 hPa composited vertical p velocity averaged over the same region. Associated with the marked increase of the upper level wind convergence on day −4 is an intensification in the subsidence at 500 hPa. Between day −4 and day +1, vertical p velocities are greater than 0.075 Pa s, which is at least 0.025 Pa s greater than the climatological summertime average of 0.05 Pa s^{-1}. This is a 50–90% increase in the strength of the subsidence over this region.

[55] Figure 13 illustrates the direct secondary circulation over the eastern Mediterranean Sea and northeastern Africa when the upper level amplification is strong on day −4 (Figure 13a) and when the upper level pattern has relaxed on day +2 (Figure 13b). Compared with day +2, subsidence is stronger over the Mediterranean Sea (32–40°N), while rising vertical motions between 900 hPa and 300 hPa over the southern Sahara and Sahel (15–25°N) are 0.01–0.02 Pa s stronger on day −4. The subsidence over the Mediterranean Sea constitutes the down branch of the direct secondary circulation, while the rising vertical motions over the southern Sahel and Sahara may form the up branch. Note that rising motion over the Sahel is not purely due to the direct secondary circulation, as the monsoon circulation to the south also strongly influences vertical motions during the summer [*Zhang et al.*, 2006]. Idealized modeling work beyond the scope of this study is needed to determine the relative contribution of rising motions over the eastern Sahel owing to the indirect circulation as opposed to upward motions associated with the African monsoon system or other forcing mechanisms. The ageostrophic meridional winds in the upper troposphere between 100–200 hPa are southerly, with magnitudes approximately 40% stronger on day −4 and covering a greater area, from 5–45°N than on day +2. Completing the direct secondary circulation is ageostrophic northerly flow at low levels. Over the Sahara (20–30°N) low-level ageostrophic northerly flow is stronger and deeper on day −4, compared to day +2. It is this intensification of the low-level northerly flow that is asso-

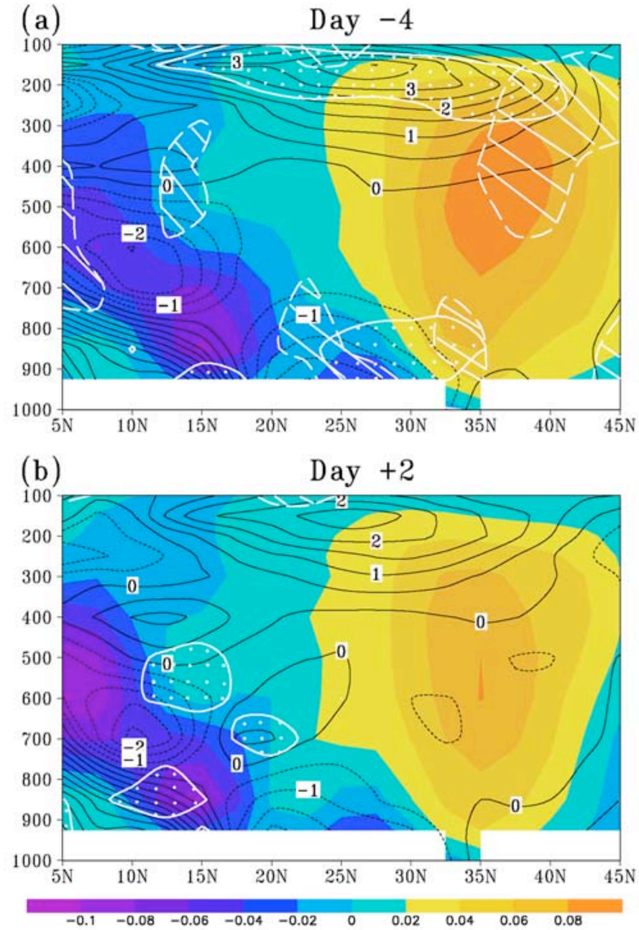

Figure 13. Composite vertical p velocity (shaded) and ageostrophic meridional wind component (contoured) averaged between 10 and 30°E for (a) day −4 and (b) day +2. Contour interval is every 0.5 m s^{-1}, while shading interval is every 0.02 Pa s. Hatched (stippled) regions denote where the vertical p velocity (ageostrophic meridional wind) is significant at the 95% level.

ciated with the equatorward movement of the cold air surge over northeastern Africa (e.g., Figure 3).

[56] The position of the direct circulation's subsidence center on day −4 (Figure 13a) is on the cyclonic shear side of the jet close to the jet core axis, and the rising branch is well south of the jet axis at between 10 and 15°N (Figure 11b). This differs from classical straight jet streak theory [e.g., *Keyser and Shapiro*, 1986] which suggests that these regions should straddle the jet-core axis. As inferred from the composite temperature and wind vector fields in Figure 11b, the relative equatorward positioning of the direct circulation in the jet entrance region on day −4 is associated with both along jet cold air advection over the central Mediterranean Sea and thermal ridging associated with curvature effects related to the upper level anticyclone over the Middle East and South Asia (Figure 2d).

6. Conclusions

[57] Analysis of the NCEP Reanalysis 2 and TRMM rainfall data for the summers of 1998–2006 shows that low-level cold air surges occur over northern Africa during the boreal summer. There are 6–10 cold air surge outbreaks per summer, with nearly 75% of the events reaching the northern Sahel over eastern Africa at 17.5°N and lasting 2 to 10 days. The temperature anomalies move equatorward from the Mediterranean Sea into northern Africa at an average speed of 5.46 m s^{-1}, which is about 1.5 m s^{-1} faster than the summer climatological meridional flow.

[58] While the lower-tropospheric temperature and sea level pressure anomalies associated with the summertime African cold air surges are generally smaller in magnitude than anomalies associated with cold season surges in other regions of the world [e.g., *Boyle*, 1986; *Marengo et al.*, 1997; *Schultz et al.*, 1998; *Garreaud*, 1999], they are comparable to the South American summertime cold air surge estimates of a 4 K temperature drop and a 2 hPa pressure drop [e.g., *Garreaud and Wallace*, 1998]. For individual cases the temperature change can range from less than −1 K to over −6 K with the coldest temperatures confined to northern Libya and Egypt. There is also a seasonal dependence, with the strongest cold air surges occurring earlier in the summer (June). Twice as many cold air surge events reach the eastern Sahel (∼17.5°N) in June than in July, August, or September (Figure 3).

[59] The dynamics of cold air surges over northern Africa are similar to surges in other parts of the world, with an amplified upper tropospheric ridge/trough pattern with the ridge (trough) axis centered over northwestern Africa (over the eastern Mediterranean Sea), a hydrostatically induced ridge of surface pressure, and strong meridional low-level flow. In a northern African surge event, the amplification of the upper level flow pattern over the Mediterranean Sea is associated with the passage of an upper level shortwave trough, a tightening of the height gradient, and an increase in upper level confluence. This is significant because the central/eastern Mediterranean Sea region coincides with the location of the jet entrance region for the upper tropospheric westerly jet streak. Associated with the stronger height gradient and confluence, the jet streak intensifies over the eastern Mediterranean Sea and western Asia, accompanied by an intensification of the direct secondary circulation in the jet entrance region (Figure 13), which is associated with an increase in upper level wind convergence and subsidence over the central and eastern Mediterranean Sea, stronger low-level (upper level) ageostrophic northerly (southerly) flow over northeastern Africa including Libya and Egypt, and stronger rising motion over the eastern Sahel on the northern flank of the continental land-based convergence zone. It is this intensification of the low-level northerly flow (called the Etesian winds) combined with the low-level summer climatological northerly flow over northeastern Africa that advects in the cooler air over northeastern Africa, while the northwest to southeast axis tilt of the northern African topography (Figure 1a) aids in the channeling of the cold air predominantly toward eastern Africa and the eastern Sahel (Figure 6).

[60] Since the topography is not an unbroken chain, there are gaps through which leakages of cold air can be observed, including over central Algeria between the Atlas and Ahaggar Mountains, and over Chad between the Tibesti and Ennedi Mountains. The low-level flow is accelerated through these gaps during cold air surge events. Leakages are

not uncommon elsewhere in the world. For example, *Schultz et al.* [1997] discussed the importance of gaps in the Central American mountains during winter cold air surge outbreaks.

[61] The Froude number and the Rossby radius of deformation for the Atlas Mountains are estimated to be 0.10 and 250 km, respectively. These estimates indicate that the topography is playing a role, though perhaps not a dominant role in the cold air surge dynamics. Future work is needed to better understand the role of the topography for cold air surge development over northern Africa.

[62] A composite is constructed from 15 summertime surge events to investigate the timing of circulation characteristics associated with northern Africa cold air surges. The 200 hPa flow amplifies into a ridge/trough pattern over the western Mediterranean Sea one week (e.g., on day −7) before the cold air reaches the eastern Sahel (∼17.5°N) in association with the development and passage of an upper level shortwave trough. The 200 hPa ridge/trough pattern achieves maximum amplification over the Mediterranean Sea on day −4, when the 200 hPa westerly jet streak and the confluence in the jet entrance region over the Mediterranean Sea are strongest. This amplified pattern breaks down first in the upper troposphere between day −2 and day 0, and then in the midtroposphere between day 0 and day +2.

[63] At low levels, the cold air surge begins to propagate equatorward over northern Africa, in particular western Libya and eastern Algeria, by day −4, coinciding with the maximum amplification of the upper tropospheric pattern and the strongest subsidence over the central Mediterranean Sea. The cold air moves southward and eastward over the next 4 days. Conditions remain cooler than normal over northeastern Africa 4 days after the surge reaches the eastern Sahel (17.5°N).

[64] The composites demonstrate that cold air surges influence the summertime synoptic variability of rainfall over northern Africa, especially over the western Sahara (20–25°N, 15°W–10°E) and the eastern Sahel (12–20°N, 15–35°E). Convective activity is enhanced over the western Sahara 2 to 5 days before the surge reaches the eastern Sahel, when northeasterly flow channeled in the gap between the Atlas and Ahaggar Mountains strengthens and transports relatively moist air from the western Mediterranean and eastern North Atlantic (Figure 9). Over the eastern Sahel, the composite results reveal a break in convective activity when the surge arrives that persists for about 6 days. The difference in the rainfall responses over the western Sahara and eastern Sahel due to cold air surges is related to the differences in the low-level moisture field in these two regions (Figure 2c) and the latitudinal extent that the cold air surge extends. The western Sahara is so dry that any change in the circulation, including those associated with a cold air surge, will be likely to increase the low-level moisture and convective instability in the region. Furthermore, the cold air surge penetrates only to 20°N over this region. Over the eastern Sahel, the cold air surge reaches 10°N. Low-level moisture values are greater owing to the moist, southwesterly flow of the African monsoon system, so increased northerly flow is associated with a decrease in moisture, and a more stable environment that favors a break in the rainfall.

[65] These results offer promise for improving short-range prediction of rainfall breaks over the eastern Sahel during boreal summer through the use of the circulation characteristics associated with cold air surges. Additional work is needed to address the relevance of the circulation mechanisms identified in this work for weaker surge events and their relationship to rainfall variability, as well as to characterize the robustness of these results in other observational data and reanalyzed data products (i.e., verify that they are not just unique to the data sets selected for this analysis). Additionally, there is evidence that the frequency of cold air surges over northern Africa may vary on monthly time scales (e.g., Figure 3), but a longer time series is needed to solidify this result. Connections between cold air surge events and the "Sahel mode" of intraseasonal variability identified by *Mounier and Janicot* [2004] and other mechanisms that are found to influence intraseasonal variability (e.g., easterly wave activity from the Indian Ocean, West African monsoon variability) also need to be explored in greater depth. In particular, the day −6 composite of the low-level wind and moisture anomalies (Figures 8a and 8b) is similar to the t_0 −6 composite for the Sahel mode (see top right of Figure 2 from *Mounier and Janicot* [2004]). Fluctuations in the low-level northerly flow, not only those associated with cold air surges, may be playing an important role in this particular mode of intraseasonal variability and need to be better understood.

[66] Finally, the decrease in frequency of strong cold air surges over northern Africa after June coincides with the decline from the June peak in the dust season for the hyperarid desert regions of North Africa [e.g., *N'tchayi Mbourou et al.*, 1997; *Engelstaedter and Washington*, 2007], suggesting a potential connection between cold air surges and dust outbreaks. Inspection of the individual cases for the summer of 2006 identified in Table 1 compared with satellite derived dust estimates from Meteosat satellite images confirms a relationship between cold air surges and dust outbreaks over northern Africa. In particular, satellite imagery suggests that cold air surges may act as a synoptic catalyst to promote dust outbreaks over the two main source regions over northern Africa, namely the Bodélé depression of Chad and the Western Saharan region of southern Algeria, Mali, and Mauritania [e.g., *Washington et al.*, 2003]. Enhanced low-level flow associated with cold air surges channels through the gaps in the topography over Algeria and northern Chad, increasing the low-level wind speeds over these dust source regions (Figure 6). Satellite imagery from the summer of 2006 confirms that there was an increase in dust activity coinciding with the increase in low-level flow through the gap between the Atlas and Ahaggar Mountains, and between the Tibesti and Ennedi Mountains. Our results are consistent with *Knippertz et al.* [2008]. In their field campaign in southern Morocco during May and June 2006, they found significant dust events over northwestern Africa were associated with cold air surge events, the channeling of low-level flow between the Atlas and Ahaggar Mountains, and particular synoptic conditions including the passage of an upper level wave. Further work is needed to investigate the role of cold air surges in forcing northern African dust outbreaks not just during the summer, but for outbreaks in other seasons. Thus, there may also be

some predictability of dust events based on a better understanding of cold air surge outbreaks.

Appendix A: Calculation of Statistical Significance for the Composites

[67] To calculate the significance for a given day of the composite, a Student's t test is employed defined by the equation below:

$$t = \frac{(\bar{x} - \mu_o)}{\left(\frac{S}{\sqrt{n}}\right)} \tag{A1}$$

[68] In equation A1, n is the sample size, in this case the 15 cold air surge events, while $\bar{x}$ is the composite mean value of the variable being tested. S is the standard deviation for the 15 events that formulate the composite. Finally, μ_o is the weighted monthly climatological value of the field. The daily mean values from the NCEP2 reanalysis between 1979 and 2006 are used to calculate climatological monthly mean values. A weighting technique is then utilized to represent μ_o and reduce effects of seasonality. In this approach, for each of the given 15 days/events that make up the composite field, $\bar{x}$, the month is noted and used to weight μ_o. For example, if the 15 events that make up the composite for a given time included 7 days in June, 4 in July, 3 in August, and 1 in September, then μ_o would be defined as

$$\mu_o = \frac{7}{15}\mathrm{Clim}_{\mathrm{June}} + \frac{4}{15}\mathrm{Clim}_{\mathrm{July}} + \frac{3}{15}\mathrm{Clim}_{\mathrm{Aug}} + \frac{1}{15}\mathrm{Clim}_{\mathrm{Sep}} \tag{A2}$$

where $\mathrm{Clim}_{\mathrm{June}}$, $\mathrm{Clim}_{\mathrm{July}}$, $\mathrm{Clim}_{\mathrm{Aug}}$, and $\mathrm{Clim}_{\mathrm{Sep}}$ are the climatological (1979–2006) monthly NCEP2 values of the field for June, July, August, and September, respectively. The degrees of freedom are n − 1, or in this case 14.

[69] **Acknowledgments.** This research was supported by NSF award ATM-0415481. The rainfall data used in this study were acquired as part of the Tropical Rainfall Measuring Mission (TRMM). The algorithms were developed by the TRMM Science Team. The data were processed by the TRMM Science Data and Information System and the TRMM Office; they are archived and distributed by the Goddard Distributed Active Archive Center. TRMM is an international project jointly sponsored by the Japan National Space Development Agency and the U.S. NASA Office of Earth Sciences. Special thanks to Sebastian Engelstaedter for processing and helping to interpret the Meteosat satellite data.

References

Beebe, R. G., and F. C. Bates (1955), A mechanism for assisting in the release of convective instability, *Mon. Weather Rev.*, *83*, 1–10, doi:10.1175/1520-0493(1955)083<0001:AMFAIT>2.0.CO;2.

Bell, M. A., and P. J. Lamb (2006), Integration of weather system variability to multidecadal regional climate change: The West African Sudan-Sahel zone, 1951–98, *J. Clim.*, *19*, 5343–5365, doi:10.1175/JCLI4020.1.

Berry, G. J., and C. Thorncroft (2005), Case study of an intense African easterly wave, *Mon. Weather Rev.*, *133*, 752–766, doi:10.1175/MWR2884.1.

Bluestein, H. B. (1993), *Synoptic-Dynamic Meteorology in Mid-Latitudes; Observations and Theory of Weather Systems*, vol. 2, Oxford Univ. Press, London.

Boyle, J. S. (1986), Comparison of the synoptic conditions in midlatitudes accompanying cold surges over eastern Asia for the months of December 1974 and 1978. Part I: Monthly mean fields and individual events, *Mon. Weather Rev.*, *114*, 903–918, doi:10.1175/1520-0493(1986)114<0903:COTSCI>2.0.CO;2.

Chang, C.-P., and K. M. W. Lau (1980), Northeasterly cold surges and near-equatorial disturbances over the winter Monex area during December 1974. Part II: Planetary-scale aspects, *Mon. Weather Rev.*, *108*, 298–312, doi:10.1175/1520-0493(1980)108<0298:NCSANE>2.0.CO;2.

Chu, P.-S., and S.-U. Park (1984), Regional circulation characteristics associated with a cold surge event over east Asia during winter MONEX, *Mon. Weather Rev.*, *112*, 955–965, doi:10.1175/1520-0493(1984)112<0955:RCCAWA>2.0.CO;2.

Colle, B. A., and C. F. Mass (1995), The structure and evolution of cold surges east of the Rocky Mountains, *Mon. Weather Rev.*, *123*, 2577–2610, doi:10.1175/1520-0493(1995)123<2577:TSAEOC>2.0.CO;2.

Dallavalle, J. P., and L. F. Bosart (1975), A synoptic investigation of anticyclogenesis accompanying North American polar air outbreaks, *Mon. Weather Rev.*, *103*, 941–957, doi:10.1175/1520-0493(1975)103<0941:ASIOAA>2.0.CO;2.

Diedhiou, A., S. Janicot, A. Viltard, P. de Felice, and H. Laurent (1999), Easterly wave regimes and associated convection over West Africa and tropical Atlantic: Results from the NCEP/NCAR and ECMWF reanalyses, *Clim. Dyn.*, *15*, 795–822, doi:10.1007/s003820050316.

Engelstaedter, S., and R. Washington (2007), Atmospheric controls on the annual cycle of North African dust, *J. Geophys. Res.*, *112*, D03103, doi:10.1029/2006JD007195.

Folland, C. K., T. N. Palmer, and D. E. Parker (1986), Sahel rainfall and worldwide sea temperatures, 1901–85, *Nature*, *320*, 602–607, doi:10.1038/320602a0.

Garcia, I. P. (1996), Major cold air outbreaks affecting coffee and citrus plantations in the eastern and northeastern Mexico, *Atmósfera*, *9*, 47–68.

Garreaud, R. D. (1999), Cold air incursions over subtropical and tropical South America: A numerical case study, *Mon. Weather Rev.*, *127*, 2823–2853, doi:10.1175/1520-0493(1999)127<2823:CAIOSA>2.0.CO;2.

Garreaud, R. D. (2000), Cold air incursions over subtropical South America: Mean structure and dynamics, *Mon. Weather Rev.*, *128*, 2544–2559, doi:10.1175/1520-0493(2000)128<2544:CAIOSS>2.0.CO;2.

Garreaud, R. (2001), Subtropical cold surges: Regional aspects and global distribution, *Int. J. Climatol.*, *21*, 1181–1197, doi:10.1002/joc.687.

Garreaud, R. D., and J. M. Wallace (1998), Summertime incursions of mid-latitude air into tropical and subtropical South America, *Mon. Weather Rev.*, *126*, 2713–2733, doi:10.1175/1520-0493(1998)126<2713:SIOMAI>2.0.CO;2.

Hartjenstein, G., and R. Bleck (1991), Factors affecting cold-air outbreaks east of the Rocky Mountains, *Mon. Weather Rev.*, *119*, 2280–2292, doi:10.1175/1520-0493(1991)119<2280:FACAOE>2.0.CO;2.

Hodges, K. I., and C. D. Thorncroft (1997), Distribution and statistics of African mesoscale convective weather systems based on the ISCCP METEOSAT imagery, *Mon. Weather Rev.*, *125*, 2821–2837, doi:10.1175/1520-0493(1997)125<2821:DASOAM>2.0.CO;2.

Huffman, G. J., R. F. Adler, D. T. Bolvin, G. Gu, E. J. Nelkin, K. P. Bowman, Y. Hong, E. F. Stocker, and D. P. Wolff (2007), The TRMM multisatellite precipitation analysis (TMPA): Quasi-global, multiyear, combined-sensor precipitation estimates at fine scales, *J. Hydrometeorol.*, *8*, 38–55, doi:10.1175/JHM560.1.

Janicot, S., and B. Sultan (2001), Intraseasonal modulation of convection in the West African monsoon, *Geophys. Res. Lett.*, *28*, 523–526, doi:10.1029/2000GL012424.

Janicot, S., S. Trzaska, and I. Poccard (2001), Summer Sahel-ENSO teleconnection and decadal time scale SST variations, *Clim. Dyn.*, *18*, 303–320, doi:10.1007/s003820100172.

Kanamitsu, M., W. Ebisuzaki, J. Woollen, S. K. Yang, J. J. Hnilo, M. Fiorino, and G. L. Potter (2002), NCEP-DOE AMIP-II reanalysis (R2), *Bull. Am. Meteorol. Soc.*, *83*, 1631–1643, doi:10.1175/BAMS-83-11-1631(2002)083<1631:NAR>2.3.CO;2.

Keyser, D., and M. A. Shapiro (1986), A review of the structure and dynamics of upper-level frontal zones, *Mon. Weather Rev.*, *114*, 452–499, doi:10.1175/1520-0493(1986)114<0452:AROTSA>2.0.CO;2.

Kiladis, G. N., and K. M. Weickmann (1997), Horizontal structure and seasonality of large-scale circulations associated with submonthly tropical convection, *Mon. Weather Rev.*, *125*, 1997–2013, doi:10.1175/1520-0493(1997)125<1997:HSASOL>2.0.CO;2.

Knippertz, P., et al. (2008), Dust mobilization and transport in the northern Sahara during SAMUM 2006: A meteorological overview, *Tellus*, *61B*, doi:10.1111/j.1600-0889.2008.00380.x.

Konrad, C. E., II (1996), Relationship between the intensity of cold-air outbreaks and the evolution of synoptic and planetary-scale features over North America, *Mon. Weather Rev.*, *124*, 1067–1083, doi:10.1175/1520-0493(1996)124<1067:RBTIOC>2.0.CO;2.

Kousky, V. E. (1979), Frontal influences on northeast Brazil, *Mon. Weather Rev.*, *107*, 1140–1153, doi:10.1175/1520-0493(1979)107<1140:FIONB>2.0.CO;2.

Kousky, V. E., and I. Cavalcanti (1997), The principle modes of high-frequency variability over the South American region, paper presented at 5th International Conference on Southern Hemisphere Meteorology and Oceanography, Am. Meteorol. Soc., Pretoria, South Africa.

Krishnamurti, T. N., M. Tewari, D. R. Chakraborty, J. Marengo, P. L. Silva Dias, and P. Satyamurty (1999), Downstream amplification: A possible precursor to major freeze events over southeastern Brazil, *Weather Forecasting*, *14*, 242–270, doi:10.1175/1520-0434(1999)014<0242:DAAPPT>2.0.CO;2.

Laing, A. G., and J. M. Fritsch (1993), Mesoscale convective complexes in Africa, *Mon. Weather Rev.*, *121*, 2254–2263, doi:10.1175/1520-0493(1993)121<2254:MCCIA>2.0.CO;2.

Lamb, P. J. (1978), Large-scale tropical Atlantic surface circulation patterns associated with sub-Saharan weather anomalies, *Tellus*, *30*, 240–251.

Lau, K.-M., C.-P. Chang, and P. H. Chan (1983), Short-term planetary-scale interactions over the tropics and midlatitudes. Part II: Winter-MONEX period, *Mon. Weather Rev.*, *111*, 1372–1388, doi:10.1175/1520-0493(1983)111<1372:STPSIO>2.0.CO;2.

Lavaysse, C., A. Diedhiou, H. Laurent, and T. Lebel (2006), African easterly waves and convective activity in wet and dry sequences of the West African monsoon, *Clim. Dyn.*, *27*, 319–332, doi:10.1007/s00382-006-0137-5.

Liebmann, B., G. Kiladis, J. Marengo, T. Ambrizzi, and J. D. Glick (1999), Submonthly convective variability over South America and the South Atlantic convergence zone, *J. Clim.*, *12*, 1877–1891, doi:10.1175/1520-0442 (1999)012<1877:SCVOSA>2.0.CO;2.

Marengo, J., A. Cornejo, P. Satymurty, C. Nobre, and W. Sea (1997), Cold surges in tropical and extratropical South America: The strong event in June 1994, *Mon. Weather Rev.*, *125*, 2759–2786, doi:10.1175/1520-0493(1997)125<2759:CSITAE>2.0.CO;2.

Mathon, V., and H. Laurent (2001), Life cycle of Sahelian mesoscale convective cloud systems, *Q.J.R. Meteorol. Soc.*, *127*, 377–406, doi:10.1002/qj.49712757208.

Matthews, A. J. (2004), Intraseasonal variability over tropical Africa during northern summer, *J. Clim.*, *17*, 2427–2440, doi:10.1175/1520-0442(2004)017<2427:IVOTAD>2.0.CO;2.

Mounier, F., and S. Janicot (2004), Evidence of two independent modes of convection at intraseasonal timescale in the West African summer monsoon, *Geophys. Res. Lett.*, *31*, L16116, doi:10.1029/2004GL020665.

Mounier, F., S. Janicot, and G. N. Kiladis (2008), The West African monsoon dynamics. Part III: The quasi-biweekly zonal dipole, *J. Clim.*, *21*, 1911–1928, doi:10.1175/2007JCLI1706.1.

Murakami, T., and L. Ho (1981), Orographic influence of the Rocky Mountains on the winter circulation over the contiguous United States, *J. Meteorol. Soc. Jpn.*, *59*, 683–708.

N'tchayi Mbourou, G., J. J. Bertrand, and S. E. Nicholson (1997), The diurnal and seasonal cycles of wind-borne dust over Africa north of the equator, *J. Appl. Meteorol.*, *36*, 868–882, doi:10.1175/1520-0450(1997)036<0868:TDASCO>2.0.CO;2.

Parmenter, F. C. (1976), A Southern Hemisphere cold front passage at the equator, *Bull. Am. Meteorol. Soc.*, *57*, 1435–1440, doi:10.1175/1520-0477(1976)057<1435:ASHCFP>2.0.CO;2.

Raicich, F., N. Pinardi, and A. Navarra (2003), Teleconnections between Indian monsoon and Sahel rainfall and the Mediterranean, *Int. J. Climatol.*, *23*, 173–186, doi:10.1002/joc.862.

Rowell, D. P., C. K. Folland, K. Maskell, and M. N. Ward (1995), Variability of summer rainfall over tropical north Africa (1906–92): Observations and modelling, *Q.J.R. Meteorol. Soc.*, *121*, 669–704.

Rodwell, M. J., and B. J. Hoskins (1996), Monsoons and the dynamics of deserts, *Q.J.R. Meteorol. Soc.*, *122*, 1385–1404, doi:10.1002/qj.49712253408.

Schultz, D. M., W. E. Bracken, L. F. Bosart, G. J. Hakim, M. A. Bedrick, M. J. Dickinson, and K. R. Tyle (1997), The 1993 superstorm cold surge: Frontal structure, gap flow, and tropical impact, *Mon. Weather Rev.*, *125*, 5–39.

Schultz, D. M., W. E. Bracken, and L. F. Bosart (1998), Planetary- and synoptic-scale signatures associated with central American cold surges, *Mon. Weather Rev.*, *126*, 5–27, doi:10.1175/1520-0493(1998)126<0005:PASSSA>2.0.CO;2.

Sultan, B., S. Janicot, and A. Diedhiou (2003), The West African monsoon dynamics. Part I: Documentation of intraseasonal variability, *J. Clim.*, *16*, 3389–3406, doi:10.1175/1520-0442(2003)016<3389:TWAMDP>2.0.CO;2.

Tilley, J. S. (1990), On the application of edge wave theory to terrain bounded cold surges: A numerical study, Ph.D. thesis, Pa. State Univ., Univ. Park.

Uccellini, L. W., and D. R. Johnson (1979), The coupling of upper and lower tropospheric jet streaks and implications for the development of severe convective storms, *Mon. Weather Rev.*, *107*, 682–703, doi:10.1175/1520-0493(1979)107<0682:TCOUAL>2.0.CO;2.

Ward, M. N. (1998), Diagnosis and short-lead time prediction of summer rainfall in tropical North Africa at interannual and multidecadal timescales, *J. Clim.*, *11*, 3167–3191, doi:10.1175/1520-0442(1998)011<3167:DASLTP>2.0.CO;2.

Washington, R., M. Todd, N. J. Middleton, and A. S. Goudie (2003), Dust-storm source areas determined by the total ozone monitoring spectrometer and surface observations, *Ann. Assoc. Am. Geogr.*, *93*, 297–313, doi:10.1111/1467-8306.9302003.

Xoplaki, E., J. F. González-Rouco, and J. Luterbacher (2003), Mediterranean summer air temperature variability and its connection to the large-scale atmospheric circulation and SSTs, *Clim. Dyn.*, *20*, 723–739.

Zhang, C., P. Woodworth, and G. Gu (2006), The seasonal cycle in the lower troposphere over West Africa from sounding observations, *Q.J.R. Meteorol. Soc.*, *132*, 2559–2582, doi:10.1256/qj.06.23.

K. H. Cook, Jackson School of Geosciences, University of Texas at Austin, P.O. Box B,University Station, Austin, TX 78713-8902, USA.

E. K. Vizy, Institute for Geophysics, University of Texas at Austin, J. J. Pickle Research Campus, Building 196, 10100 Burnet Road (R2200), Austin, TX 78758-4445, USA. (ned@utig.ig.utexas.edu)